Algorithm Theoretical Basis Document: Volcanic Ash Algorithms–V2.0

Fred Prata[1] and Stefano Corradini[3],

[1]**Norwegian Institute for Air Research**

[2]**University of Bremen**

[3]**Istituto Nazionale di Geofisica e Vulcanologia**

[4]**University of Natural Resources and Applied Life Sciences, Vienna**

October 23, 2009

Name	Date	Reason for changes	Version
Fred Prata	19.04.2009	Initial draft	Draft
Fred Prata	20.07.2009	Second draft	v0.9
Fred Prata	07.09.2009	Version 1.0 release	v1.0
Nina Kristiansen	19.10.2009	Review	v1.1
Fred Prata	22.10.2009	Version 2.0	v2.0

Document Status Table

Abstract

This document describes the algorithms used to derive volcanic ash from infrared satellite measurements. The principle instruments used are: MODIS, AIRS, AVHRR, IASI and SEVIRI and the main wavelength region employed is the infrared window region from 8 to 12 μm. SInce there are no independent data for validation of these algorithms, a detailed intercomparison between the retrievals from different sensors is performed and a theoretical assessment is made based on instrument noise performance and sensitivity to assumed or estimated parameters needed in the retrieval. Much of the essential physics of the retrieval has already been described in the literature, so here we concentrate on the technical aspects and on the details of the retrieval products. These may be classed into two groups: qualitative ash maps (QL), which may be incorporated into other graphic products, and quantitative (QN), but not yet validated ash retrievals in units of g m^{-2}. Within the QL group of products are the ash discrimination schemes that make no attempt to retrieve geophysical quantities, but emphasize methods for reducing false-detections and false-positives. The QN group of algorithms can be used to determine total mass loadings of fine ash and have a stronger physical basis.

Contents

Chapter 1

Physical principles of ash detection in the infrared

1.1 Volcanic ash detection from satellites

The problem of detecting volcanic clouds from satellites is really a problem of discrimination. Clouds absorb, emit and scatter radiation in the visible, infrared and microwave regions of the electromagnetic spectrum. At visible wavelengths, depending on the geometry of illumination (by the Sun or using a laser light source) and the geometry of observation, clouds may appear bright or dark. This is true of clouds of water, ice, silicates (volcanic ash), wind blown dust (desert dust), smoke (e.g. from a large forest fire) or any other naturally or anthropogenically generated cloud of particles. It is sometimes very clear that a particular cloud is meteorological in origin (for example, a cloud of water droplets or ice particles, or a mixed phase cloud), but often not so clear that it is not a meteorological cloud. Figure 1.1(a)–(h) shows some satellite images of "anomalous" clouds in the atmosphere. These are daytime MODIS images that have been enhanced to provide a "true-colour" rendition of the scene. In all scenes there are meteorological clouds and clouds due to other sources: (a) a thick ash column rising above Ruang volcano (Sangihie islands, Indonesia, 125.37 °E, 2.30 °N), (b) a drifting ash and gas plume recently emitted from Karthala volcano, Comoros (11.75 °S, 43.38 °E), (c) a low-level gas (predominantly SO_2 and H_2O) from Ambrym volcano, Vanuatu (16.25 °S, 168.12 °E), (d) an ash and gas plume over snow-covered terrain from Kluchevskoi volcano, Kamchatka (56.057 °N, 160.638 °E) , (e) an ash and gas plume from Kluchevskoi, but in the summer, (f) a noxious cloud generated from an industrial accident in southern England, (g) a dust outbreak travelling westwards over the Canary Islands (28.00 °N, 15.58 °W), and (h), wind-blown ash off the coast of Iceland. These examples illustrate some of the variability found in anomalous clouds when viewed by satellites during the day. Some clouds appear almost black (Fig. 1.1f) or dark grey (Fig. 1.1h), some are as white as water/ice clouds (Fig. 1.1c and 1.1d), while others take various sandy shades with brown and yellow hues (Fig. 1.1a, b, e and g). By using objective analysis of daytime visible imagery alone, it has been very difficult to unambiguously discriminate ash clouds from other clouds. During the nighttime, the task is made even more difficult. This is the main reason why infrared data has proven to be of great use. There are now several ash detection algorithms in use or proposed, based on IR and visible satellite

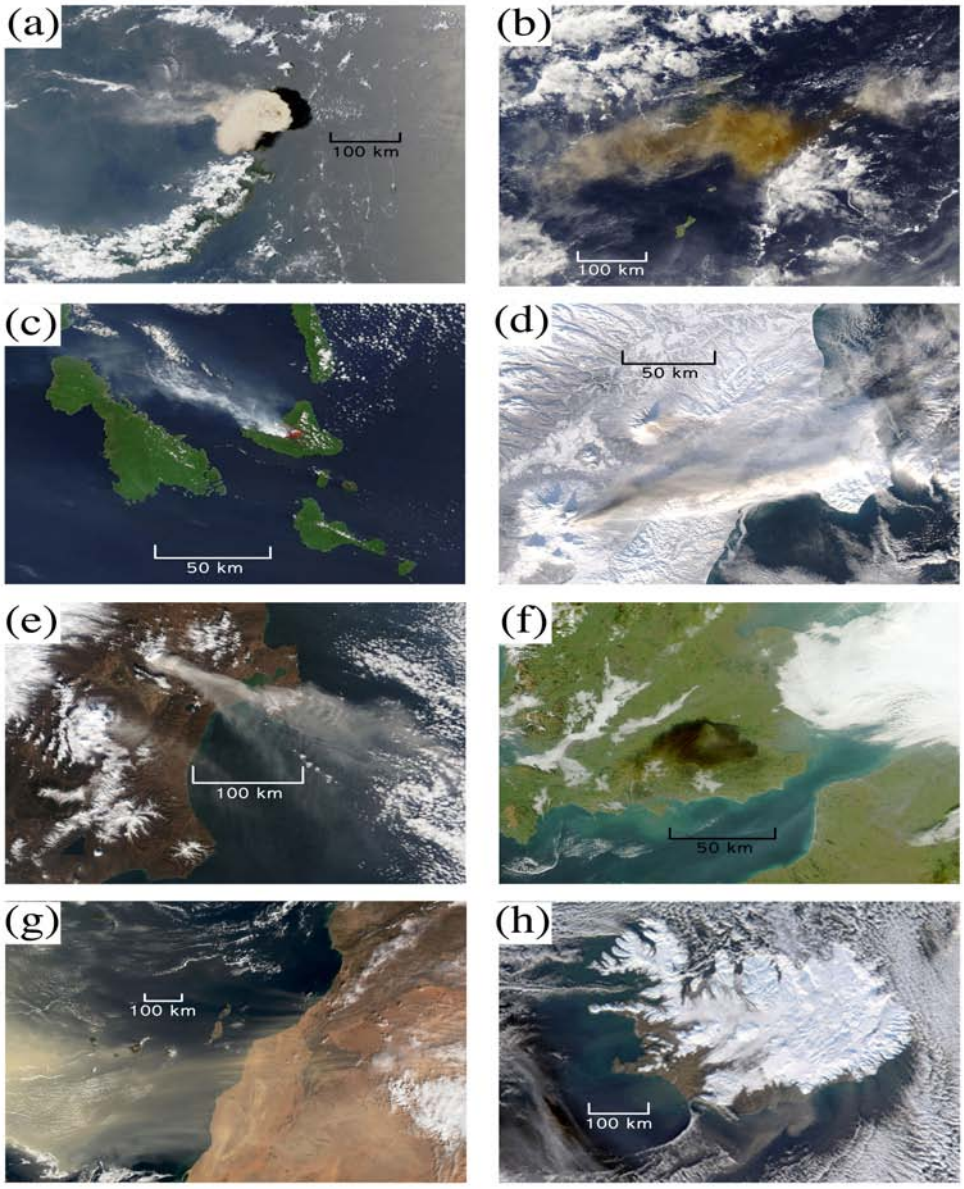

Figure 1.1: Daytime MODIS scenes showing ”anomalous” clouds. (a) Thick ash column from Ruang volcano, (b) drifting ash and gas plumes from Karthala volcano, (c) low-level gas cloud plume , (d) ash and gas plume over snow covered terrain (Kluichevskoi volcano), (e) ash and gas plume from Kluichevskoi during the summer, (f) a noxious gas cloud from an industrial fire in southern England, (g) a dust outbreak over the Canary islands, and (h) wind blown ash streaming off the southern coast of Iceland.

data. Table 1.1 shows a summary of ash detection schemes (with original references), based mostly on using infrared channels.

Name	Principle	Reference
RA	2-band IR (11 and 12 μm)	Prata (1989a,b)
Ratio	2-band IR (11 and 12 μm)	Holasek and Rose (1991)
4-Band	IR+Visible	Mosher (2000)
TVAP	3-band IR (3.9, 11 and 12 μm)	Ellrod *et al.* (2003)
PCI	Multi-band principal components	Hilger and Clark (2002a; 2002b)
WVC	2-band IR+water vapour correction	Yu *et al.* (2002)
RAT†	3-band IR (3.5, 11, 12 μm)	Pergola *et al.* (2004)
3-Band	3-band (IR and Visible)	Pavolonis *et al.* (2006)

Table 1.1: Summary of ash detection algorithms and techniques used with satellite infrared (IR) and visible channel data. (RA=Reverse Absorption; TVAP=Three-band Volcanic Ash Product; PCI=Principle Components; RAT=Ratio method; WVC=Water vapor correction method).

The two channel, reverse absorption technique is very useful in cases where the ash is not too thick and not too dispersed and is used at the VAACs (Watkin, 2003). Figure 1.2 shows an application of the technique for the eruption of Karthala (Fig. 1.1b). In this case the ash hazard is depicted using shades of yellow to red, with red suggesting more dense ash and greater hazard. Note that the white coloured clouds seen in the true colour image (Fig. 1.1b) of this event are not detected as an ash hazard. But note too that the edges of several clouds are detected as a potential ash hazard, whereas it seems more likely that these are meteorological clouds. The problems and pitfalls of using the reverse absorption technique have been discussed in the research literature (e.g. Simpson *et al.*, 2000; Prata *et al.*, 2001) and are well known to experienced meteorological analysts. Context is a key element in determining whether a particular cloud is an ash hazard or not, and trained meteorologists tasked with identifying ash clouds will use multiple sources of information including satellite imagery, pilot reports, ground observer reports, wind trajectories, and background information regarding regional volcanic activity and prior behaviour. It is possible to take the infrared analysis one step further. Wen and Rose (1994) and Prata and Grant (2001) have shown that by including a microphysical model of the ash particles with a detailed radiative transfer model, the infrared data can be inverted to reveal mean particle size and cloud opacity. When these parameters are integrated over the area covered by the cloud, the total mass and mass loading can be inferred from the data. These are quantifiable products that may be incorporated with dispersion models to generate risk maps for use by the aviation industry. An example of this kind of retrieval is given in Figure 1.3, also for the Karthala eruption.

There are many satellites (polar and geosynchronous) that carry these infrared channels, so this product can be delivered globally. Table 1.2 gives details of some of the satellite instruments capable of providing ash mass loadings.

Two of the instruments listed in Table 1.2 are capable of measuring much more than ash mass loadings. These instruments, AIRS and IASI have high spectral resolution and by utilising more measurement channels it may be possible to infer something about the mineralogy of the ash. Indeed it may also be possible to discriminate dust (Fig. 1.1g) and wind blown ash (Fig. 1.1h) outbreaks from

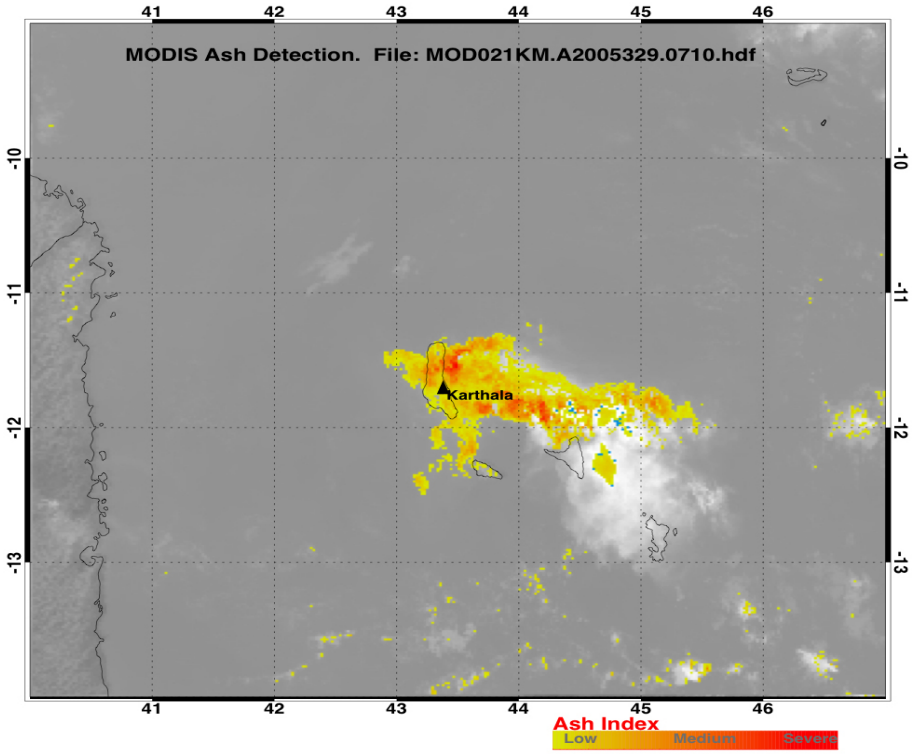

Figure 1.2: An ash ”risk” map for the Karthala eruption shown in Fig. 1.1b, based on the reverse absorption technique using two infrared channels. Regions of greatest risk are coloured red. Grey regions are believed to be “ash free”.

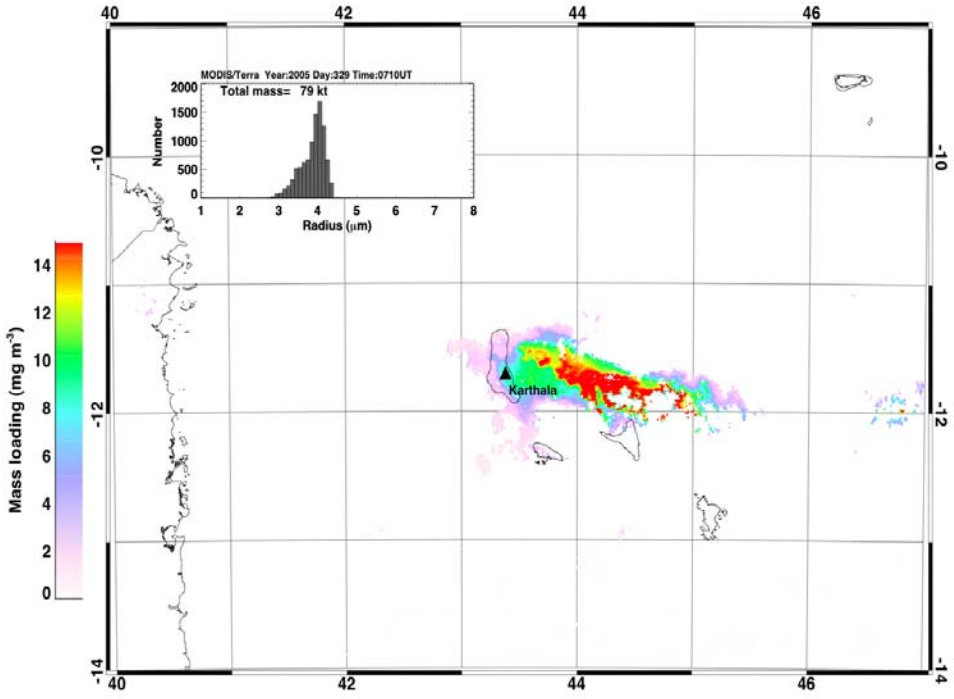

Figure 1.3: Ash mass loading retrievals for the Karthala eruption shown in Fig. 1.1b.

Satellite	Instrument	Spatial resolution (km x km)	Temporal resolution (per day)	Time period covered
NOAA	AVHRR-2, -3	1 x 1	2	1981-present
NOAA	HIRS,-2, -3,-4	10 x 10[1]	2	1979-present
GOES	VISSR/VAS	5 x 5	24	1980-present
ENVISAT	ATSR-family	1 x 1	2[2]	1991-present
GMS-5	VISSR	5 x 5	24	1995-present
Terra/Aqua	MODIS	1 x 1	4[3]	1999-present
Aqua	AIRS	14 x 14	2	2002-present
MetOp	IASI	12 x 12	2	2007-present
MSG	SEVIRI	3 x 3	96	2006-present

Table 1.2: Details of past and current satellite instruments that can be used to detect ash and generate ash mass loading maps from infrared measurements.
[1]Earlier HIRS (1–3) instruments had a larger field of view of 18 x 18 km[2]
[2]These satellite are in a 3-day repeat cycle, such that the same point imaged twice in one day will not be imaged again until 3 days later.
[3]Assuming two satellites in orbit at any given time

volcanic ash eruption clouds and plumes.

In this document the main schemes for utilising infrared data for ash detection, discrimination and quantification are described. Chapter 2 provides the salient details of the satellite and instruments employed. Chapter 3 outlines the volcanic ash model used–since satellite data alone are not sufficient to provide quantitative retrievals, a microphysical model of ash optical properties is required. Chapter 4 lists the products and their definitions and suggests a delivery mechanism. A brief validation plan is also included (Chapter 5), with more details provided in the separate SAVAA validation document. The final chapter (Chapter 6) describes the scheme to provide an "ash alert", based on the RA method for the multispectral thermal imagers (e.g. SEVIRI) and the Concavity method for the high-spectral resolution instruments (e.g. IASI).

Appendix I lists the acronyms used in the document.

Chapter 2

Satellite instrument specifics

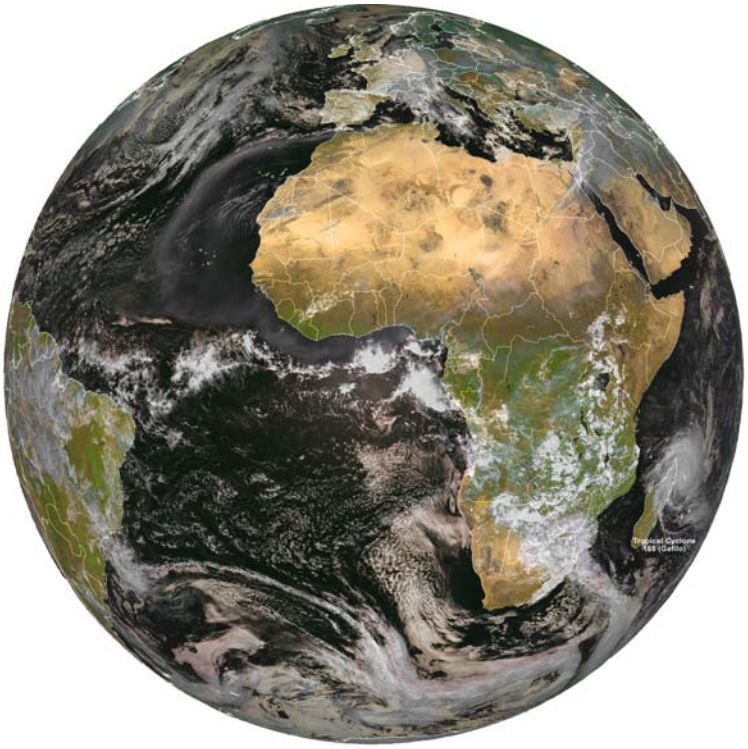

MSG view of the African continent and Europe.

Different satellite instruments provide different capabilities for ash detection because of the spectral domains covered, the temporal sampling (polar *vs.* geosynchronous), and the spatial resolution. Consideration must also be given to the operational aspects of different instruments; for example, the AVHRRs and SEVIRI are considered as operational instruments, whereas (A)ATSR and AIRS are research instruments. Nevertheless, the instruments considered here can all provide ash products with some, albeit limited, operational capability. Table 2.1 provides an overview of the capabilities of the instruments and the ash products determined from them.

Instrument	Product Freq. (per day)	Product Name	Ash Products
AVHRR-2, -3	4	AVHBTD_IR_ASH	Map: AVHBTD_IR_ASH_map Particle size: AVHBTD_IR_ASH_ps Mass: AVHBTD_IR_ASH_mass Optical depth: AVHBTD_IR_ASH_od
MODIS	4	MODBTD_IR_ASH	Map: MODBTD_IR_ASH_map Particle size: MODBTD_IR_ASH_ps Mass: MODBTD_IR_ASH_mass Optical depth: MODBTD_IR_ASH_od
(A)ATSR	2/3	ATSBTD_IR_ASH	Map: ATSBTD_IR_ASH_map Particle size: ATSBTD_IR_ASH_ps Mass: ATSBTD_IR_ASH_mass Optical depth: ATSBTD_IR_ASH_od
SEVIRI	24	SEVBTD_IR_ASH	Map: SEVBTD_IR_ASH_map Particle size: SEVBTD_IR_ASH_ps Mass: SEVBTD_IR_ASH_mass Optical depth: SEVBTD_IR_ASH_od
AIRS	2	AIRBTD_IR_ASH	Map: AIRBTD_IR_ASH_map Particle size: AIRBTD_IR_ASH_ps Mass: AIRBTD_IR_ASH_mass Optical depth: AIRBTD_IR_ASH_od

Table 2.1: Satellite instruments and ash products.

2.1 AVHRR

AVHRR data are received at the NILU EumetCast station in Kjeller, Norway. Data received are processed using standard algorithms to obtain calibrated, geolocated brightness temperatures for channels 4 (11 μm) and 5 (12 μm). A first level product is generated by channel differencing after applying a water vapour correction (Yu *et al.*, 2002). The water vapour correction is scene and climatology based and does not require any real-time data, although improvements can be made to this by using meteorological analysis data. The corrected brightness temperature differences (BTDs) are plotted onto a geographical map and a relative scale applied. The scale is intended as indicative only and

is normalized by dividing the differences by -10 K and multiplying by 100 to obtain an index in %. Differences greater than 0 K are set to 0. The resulting "ash index" runs from 0 to 100 (values greater than 100% are capped at 100%). Higher values are interpreted as more ash and hence more danger. The processing of normalization allows a consistent index to be displayed and also allows inter-comparison between different instruments. An example of this product is shown in the left panel of Figure 2.1.

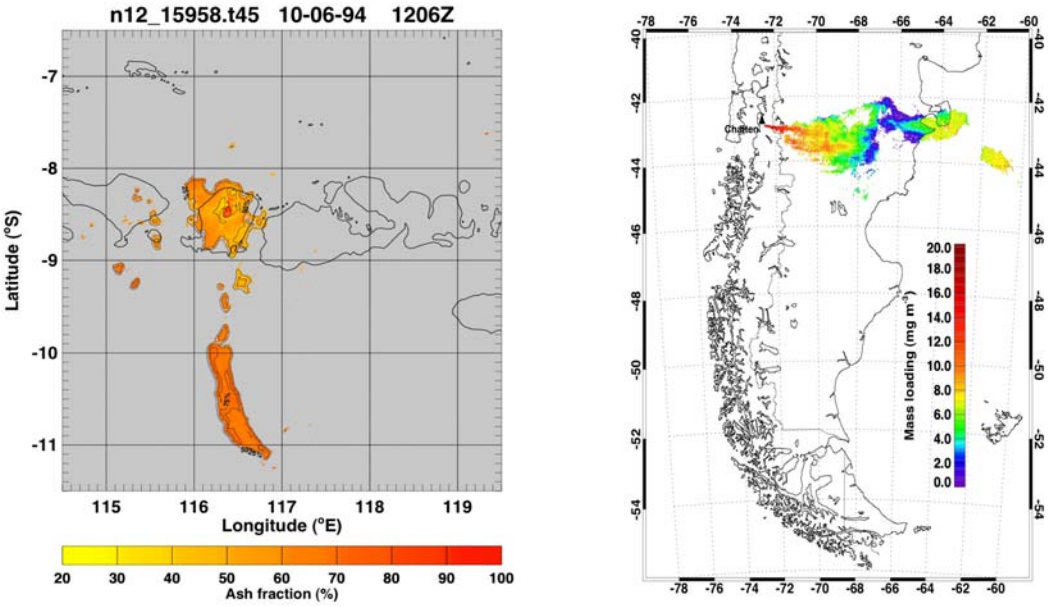

Figure 2.1: *Left panel* Ash fraction product determined from AVHRR data for a low-level eruption of Rindjani, Indonesia. *Right panel* Ash retrievals (in mg m^{-3}) from MODIS data for the eruption of Chaiten, Chile.

2.2 MODIS

Essentially the same procedures are used to obtain ash products from MODIS as those used for the AVHRRs. MODIS data are not received on the Eumetcast system, but are downloaded from the NASA DAACs or from the near real-time "rapidifire" website service. This inevitably causes some delay (several hours) in production. MODIS brightness temperatures and geolocation information are easily determined from the HDF files. As there are more spectral channels available from MODIS, it is possible to do better ash detection and also to simultaneously determine SO_2. A typical ash mass retrieval from MODIS is shown in the right-hand panel of Figure 2.1

2.3 SEVIRI

The SEVIRI instrument has several channels useful for ash detection, but for consistency with the AVHRR and MODIS instruments, only the channels at 11 μm and 12 μm are used. These data are received at NILU via the Eumetcast system and up to 96 images per day can be processed. SEVIRI data have better temporal resolution but poorer spatial resolution than either AVHRR or MODIS. Products are planned to be delivered at 1 hour intervals, but it will be possible to obtain products at the highest sampling rate of 4 per hour during explosive eruption episodes. Processing procedures to obtain brightness temperatures and geolocation information are described in various MSG documents.

2.4 (A)ATSR

The (A)ATSR data are received from the University of Leicester through a special consortium arrangement. These data cannot be obtained in near real-time and so will be used mostly for post analysis, inter-comparions and cross-validation. The (A)ATSR products (GBTs) consist of calibrated, geolocated data and these can be used directly with the ash retrieval code described later. The main difference between these data and AVHRR or MODIS is that there is an extra view (the forward view) available which may help constrain the retrievals and also provides information on ash cloud top height. No cloud height product is planned but it will be possible to use the methods described by Prata and Turner (1999) to estimate cloud top heights and compare these, on a case by case basis, with inversion results.

2.5 AIRS

Unlike the previous instruments, AIRS contains high resolution spectral information, albeit at a reduced spatial resolution. Initially it is planned to use the spectra to create "pseudo" AVHRR or MODIS brightness temperatures which can be directly inserted in the Volcanic Ash Model (VAM; see later for a description). Global AIRS data can be downloaded from the NASA DAACs in near real-time (perhaps 3–6 hours delay) and routines have been developed to determine brightness temperature spectra and to geolocate the data. Having determined "pseudo" channels it is a simple matter to use these in the VAM. As with AVHRR, MODIS and SEVIRI, ash mass, particle size and infrared optical depth will be determined for each image granule (2 per day on average).

2.6 IASI

IASI data are also high spectral resolution measurements and are recieved via the Eumetcast service. Currently software is not in place to transform the spectra into geolocated brightness temperatures, but a strong collaboration has been established with the Free University of Brussells who have the capability to transform the data into quantities needed for the VAM.

Chapter 3

Volcanic Ash Model

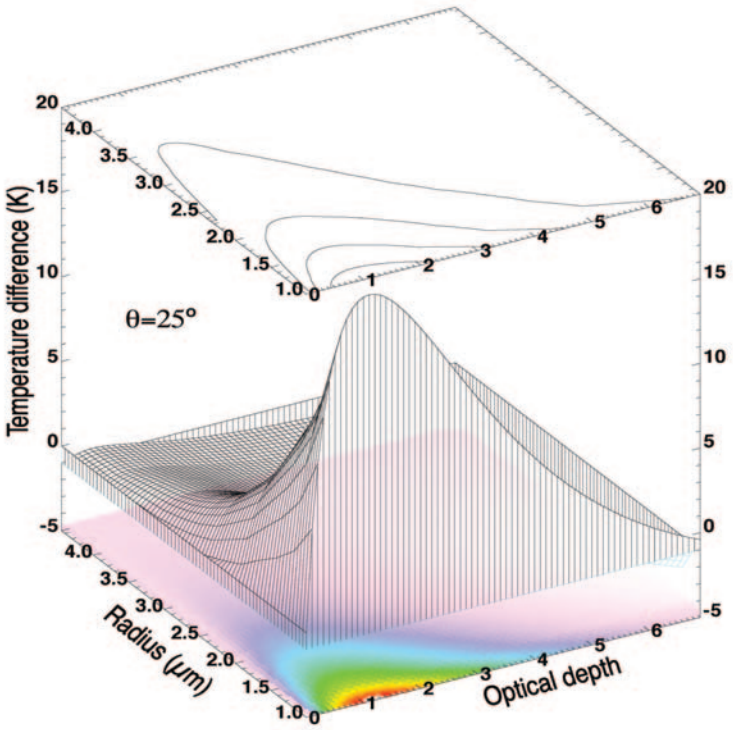

Solution space for the ash retrieval method utilising brightness temperature differences.

3.1 Retrieval method

The radiative transfer required to extract quantitative information from infrared window radiances (8–12 μm) employs Mie theory and plane parallel radiative transfer in an absorbing and scattering cloud. Given the real and imaginary parts of the index of refraction of the ash-cloud particle as a function of wavelength, and the particle shape and size distribution, the efficiencies for scattering, absorption and extinction are calculated using a Mie scattering program. There is scant information on particle shapes in real ash clouds and only approximate methods exist for calculating efficiencies for particles of arbitrary shapes. We assume that the particles are spherical and the exact Mie-theory computer program of Evans (1988) is employed to calculate the efficiencies. Some measurements exist for the particle size distribution at the edges of the Mt. St. Helens ash cloud (see the papers in Newell and Deepak, 1982). These data indicate that a log-normal (or Zold) size distribution gives a reasonable fit to the distribution. The measurements reported by King *et al.,* (1984) and Hoffman and Rosen (1984) of the El Chichón stratospheric aerosol layer fit a modified-γ size distribution quite well. These data generally pertain to volcanic aerosol layers that are relatively old and high in the atmosphere. For this work, where only the fine particles can be detected in the nascent and low (tropospheric) volcanic plumes, we assume that the size distributions would be similar. We used both size distributions (Zold and γ) to perform the radiative transfer calculations, and although there were differences in detail between the results for the two distributions, the basic results and mass loadings were essentially the same.

The parameters used in the Mie program are described in Prata (1989b). Once the Mie program has been run for each value of the size parameter (mean particle size and monochromatic wavelength), scattering parameters are then fed into a plane-parallel discrete ordinates radiative transfer program (Stamnes and Swanson, 1981). Given the single scattering albedo, asymmetry parameter, extinction and scattering efficiencies as a function of monochromatic wavelength, and the cloud-top and surface temperatures, radiances emerging from the top of the cloud along n distinct streams (zenith angles) are computed. These radiances are calculated for cloud optical depths ranging from 0 to 20 at wavelengths corresponding to AVHRR-2 channels 4 and 5, and ATSR-2 11 μm and 12 μm channels. At the completion of these calculations, a large two-dimensional look-up table exists with entries at prescribed values of the mean particle size r_m and optical depth τ. Each entry in the table consists of pairs of brightness temperatures T_4 and T_5. The retrieval then consists of locating the (r_m, τ) pairs within the look-up table that best match (T_4, T_5) pairs of AVHRR-2, MODIS, SEVIRI or (A)ATSR measurements at each image pixel. Similar schemes have been employed previously by Wen and Rose (1994) and Prata and Grant (2001).

The calculations were performed assuming that there is no absorption of infrared radiation by water vapour. This is not correct, but the effect of water vapour absorption on the results is small for the volcanic plumes studied here. The effects of atmospheric water vapour absorption on the satellite brightness temperatures have been assessed by performing radiative transfer calculations. The radiative transfer model Modtran 3 (Berk *et al.*, 1989), was used to calculate the temperature difference between the satellite measured brightness temperatures at 11 μm and 12 μm wavelengths, at each vertical level using the temperature and moisture structure from a nearby radiosonde profile.

The effect of water vapour is greatest at the lowest levels, where it exceeds 1 K. At higher levels, near to the location of the plume, the effect is less than 0.2 K. In the tropics and in high humidity conditions,

the effect of water vapour absorption can mask out the 'reverse' absorption effect of volcanic ash clouds. This can lead to misidentification of volcanic clouds and is a limitation of the current thermal detection method.

3.1.1 Size distributions, scattering parameters and mass loading

The modified-γ distribution has the functional form,

$$n(r) = N_o \frac{r^\alpha}{\Gamma[\frac{\alpha+1}{\gamma}]} b^{\frac{\alpha+1}{\gamma}} \exp(-br^\gamma), \tag{3.1}$$

where $n(r)$ is the number of particles per unit volume, r is the particle radius, Γ is the Gamma function (see Press *et al.*, 1986, page 156), N_o, b, α, and γ are parameters of the distribution. The size parameter, x, is related to the particle radius and the wavelength λ through,

$$x = \frac{2\pi r}{\lambda}. \tag{3.2}$$

Used here, γ=1, α=6, $b = 6/r_o$, and (3.1) reduces to,

$$n(x) = Cx^6 \exp\left(-\frac{6x}{x_o}\right),$$

where C is a constant replacing the other parameters. Within a distribution of sizes, the mode radius r_o corresponds to a mode size parameter x_o.

The log-normal distribution is described by,

$$n(x) = N_o \frac{1}{\sigma_x} \exp\left[-\frac{(Ln(x) - Ln(x_o))^2}{2\sigma_x^2}\right], \tag{3.3}$$

where, as before x is the size parameter. The parameter $\sigma_x = 2\pi\sigma_r/\lambda$ is related to the standard deviation (σ_r) of the distribution and is a measure of its spread. In the calculations performed with this distribution, σ_r was set to 0.5, 0.75, 1.0 and 1.25 μm, and results are reported for σ_r=1.0 μm.

The inputs to the Mie program are the real and imaginary parts of the refractive index (m), the size parameter and the size distribution. The outputs are the extinction efficiency ($\hat{Q}_{ext}$) and scattering efficiency ($\hat{Q}_{sca}$) and phase function ($P(\theta)$). For polydispersions these efficiency factors are related to the single particle efficiencies (Q_f)by,

$$\hat{Q}_f = \frac{\int_o^\infty \pi r^2 Q_f(\frac{2\pi r}{\lambda}, m) \frac{dn(r)}{dr} dr}{\int_o^\infty \pi r^2 \frac{dn(r)}{dr} dr}. \tag{3.4}$$

The absorption efficiency is,

$$\hat{Q}_{abs} = \hat{Q}_{ext} - \hat{Q}_{sca}. \tag{3.5}$$

The remaining parameters that are needed to perform the radiative transfer calculations and which relate to the cloud microphysical structure are: The single scattering albedo,

$$\varpi = \frac{\hat{Q}_{ext}}{\hat{Q}_{sca}}, \tag{3.6}$$

the asymmetry parameter,

$$g = \frac{1}{2}\int_{-1}^{1} P(\theta)\cos\theta d\cos\theta, \tag{3.7}$$

where θ is the scattering angle. The number of particles per unit volume in the cloud is,

$$N = \int_{o}^{\infty} \frac{dn}{dr} dr, \tag{3.8}$$

and the optical depth of the cloud is,

$$\tau_\lambda = \pi L \int_{o}^{\infty} r^2 Q_{ext}(r,\lambda) n(r) dr, \tag{3.9}$$

where L is the geometrical thickness of the cloud. The mass loading (kg m^{-3}) is

$$M = \frac{4\pi}{3}\rho \int_{o}^{\infty} r^3 n(r) dr, \tag{3.10}$$

where ρ is the density of the ash. The total mass can be calculated by multiplying (3.10) by the volume of a pixel (geometric thickness multiplied by the area of a pixel).

3.1.2 Retrieval procedure

Designating the brightness temperatures in the shorter wavelength channel as T_4 and those in the longer wavelength channel as T_5[1], then in the (T_4, $T_4 - T_5$) plane there exist isolines of constant mean particle radius, r_m^j. Each point on the isoline, r_m^j corresponds to particular values of the optical depth, $\tau^{j,i}$. Lines connecting equal values of $\tau^{j,i}$ also exist. Given the measured values (T_4^*, T_5^*), the retrieval procedure requires us to find the 'best' values of (τ, r_m). A linear interpolation procedure is adopted:

- Find values of $T_4(\tau^{j,i}, r_m^j)$ that bracket T_4^*. Label these $T_4^1(r_m^j)$, $T_4^2(r_m^j)$,$T_4^1(r_m^{j+1})$,$T_4^2(r_m^{j+1})$
- Interpolate on the r_m^j isolines to find the appropriate $\Delta T^(r_m^j)$ ($= T_4(r_m^j) - T_5(r_m^j)$).

$$\Delta T(r_m^j) = w_1 \Delta T_2(r_m^j) + (1 - w_1)\Delta T_1(r_m^j),$$

$$w_1 = \frac{T_4^1(r_m^j) - T_4^*}{T_4^1(r_m^j) - T_4^2(r_m^j)}.$$

  Similarly for $\Delta T(r_m^{j+1})$:

$$\Delta T(r_m^{j+1}) = w_2 \Delta T_2(r_m^{j+1}) + (1 - w_2)\Delta T_1(r_m^{j+1}),$$

  and the weight w_2 is defined in an analogous way to w_1.

[1]This terminology arises from the common usage of AVHRR channels 4 and 5. For MODIS the equivalent band numbers are 31 and 32.

- The required mean particle radius is obtained using linear interpolation,

$$r_m^* = w_r r_m^j + (1 - w_r) r_m^{j+1},$$
$$w_r = \frac{\Delta T(r_m^{j+1}) - \Delta T^*}{\Delta T(r_m^{j+1}) - \Delta T(r_m^j)}.$$

- In practice there are n isolines of $r_m^j, j = 1, n$ and n is small ($n = 18$), and many more values of $\tau^{j,i}, i = 1, k$ ($k = 100$ is used in the current software). Thus $2nxk$ values of ΔT are precomputed.

3.2 Particle radius retrievals

Figure 3.1 shows a the distribution of fine ash mass and the mean particle radius retrieved from a MODIS image for the eruption of Mt Etna, Sicily The largest particles (up to ≈ 4 μm radii) are found around the middle of the plume and in 'clumps' distributed along the plume.

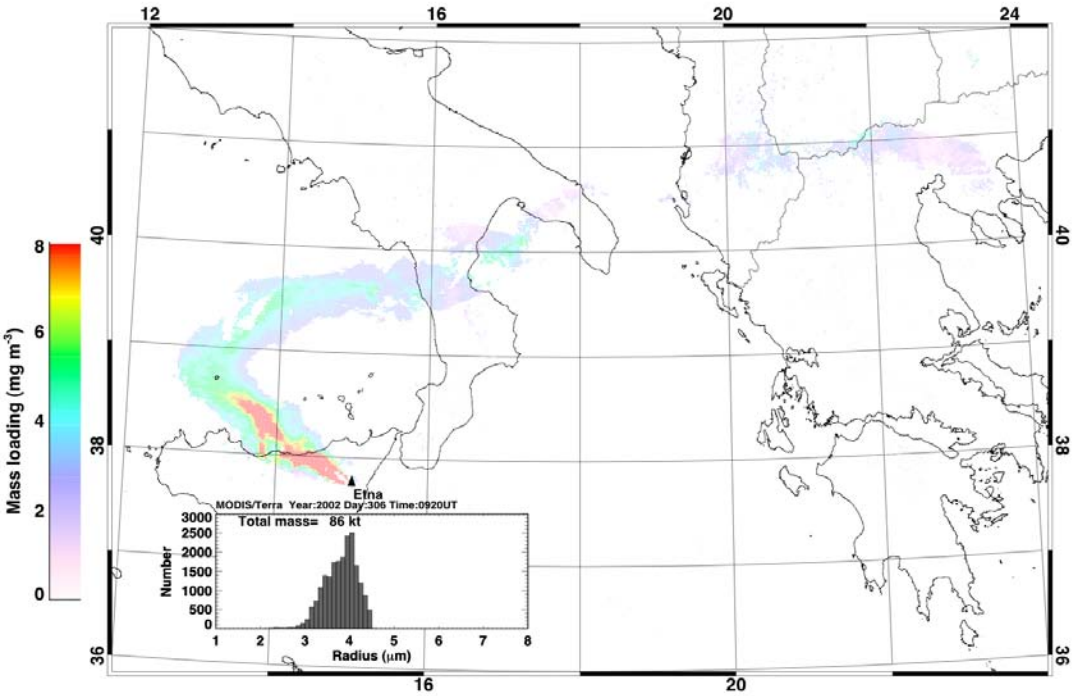

Figure 3.1: Ash mass loading (mg m^{-3}) and mean particle radius size distribution determined from 2-band MODIS thermal infrared data for an eruption of Mt Etna, Sicily.

Sometime large particles are found at the edges of these plumes and this may be an artifact of the analysis because these regions are often quite transparent and as explained previously it is possible

that the entrainment of ambient (water-rich) air may be significant. This leads to an under-constrained retrieval with larger errors. There are, however, closed contours within the plume with congregations of large particles. There appears to be an elongation of the particle size contours in the direction of the wind at that level. There also appears to be a gradient in mass loading and hence particle size from smallest particles in the at the plume edges and at greater distances from the vent, to largest particles in the centre of the plume and closest to the vent.

Figure 3.2 shows frequency distributions of particle sizes in the plumes from Mt Ruapehu, New Zealand to illusrtate the effect of using different size distribution models. Particle sizes vary from 1 μm up to $\approx$ 4 μm, with mode maxima near 3 μm. There is some evidence of multiple modes within the distribution and such behaviour has been found for the Fuego and Santiago ash clouds (Cadle *et al.*, 1979), the Mt. St. Helens ash cloud (Chuan *et al.*, 1981; Farlow *et al.*, 1981), and the Agung ash clouds (Mossop, 1964). Chuan *et al.* (1981) found a mode peak at radius $\approx$ 2.5 μm from monitoring continuous emissions from Mt. St. Helens, prior to a strong eruption on August 7 1980.

3.3 Mass loadings

The U. S. Military consider mass loadings $>$ 50 mg m^{-3} a potential hazard to their aircraft operations. Przedpelski and Casadevall (1994) estimated a mass loading of $\approx$ 2000 mg m^{-3} at 25,000 ft ($\approx$ 7.5 km) for the 15 December 1989 Redoubt eruption cloud that caused significant damage to a KLM Boeing 747-400 jet aircraft. Mass loadings include all particles with radii $<$ 50 μm, which have atmospheric residence times of the order of at least a few hours. Having determined the particle size distribution, the geometrical thickness of the cloud and its areal extent, it is possible to estimate the mass loading of fine particles in volcanic plumes.

The following discussion utilises retrievals for the 1996 eruption of Mt Ruapehu, New Zealand; for which results have been reported in the literature by Prata and Grant (2001). The density of the ash is taken to be 2600 kg m^{-3} and the area of a pixel is taken as 1.2 x 1.2 km^2 – this is a mean area for pixels for both the AVHRR-2 and ATSR-2. Pixels are counted if they satisfy criterion (6.1; see Chapter 6 "Ash Alert"), and the retrieved particle size is in the range $1 < r_m < 8$ μm. An estimate of the cloud thickness is needed to evaluate of mass loadings. Data on cloud thicknesses are not available so they must be estimated by other means. Studies of plume rise in stable stratified atmospheres (e.g. Briggs, 1975) suggest that to a reasonable approximation the vertical extent of a plume can be estimated from the cloud-top height. For example, Manins (1985) has calculated the heights and vertical extents of stabilized smoke plumes as a function of power release and following Briggs (1975) suggests that the vertical extent (cloud thickness), Δz, of these plumes is given by,

$$\Delta z = 0.4 z_{top},$$

where z_{top} is the height of the plume top. The cloud-top heights calculated previously for the Ruapehu plumes suggest a cloud thickness range of 1.5–3.0 km, with a likely error of $\pm$0.5 km. The variability of cloud thickness along the plumes and the problem of not having simultaneous plume-top height and plume-base height data for each of the plumes, means that we cannot estimate plume thickness to

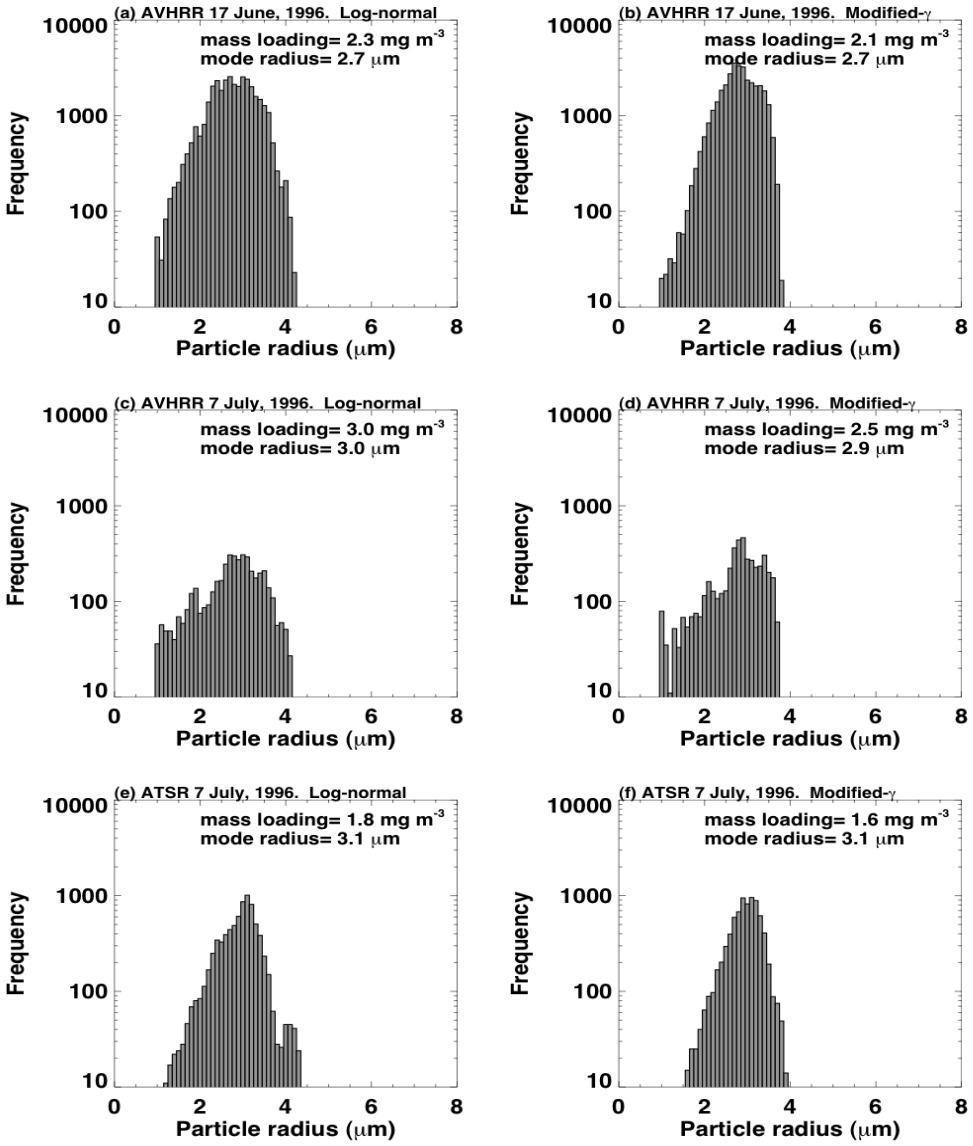

Figure 3.2: Retrieved particle size distributions for four Ruapehu plumes and two model size distributions.

any greater accuracy. The mass loading (kg m^{-3}) is

$$M = \frac{4\pi}{3}\rho \int_o^\infty r^3 n(r) dr, \tag{3.11}$$

where ρ is the density of the ash and $n(r)$ is the size distribution. The total mass can be calculated by multiplying (3.11) by the volume of a pixel (geometric thickness multiplied by the area of a pixel). Table 3.1 lists the results obtained for all four plumes using both size distributions. An alternative to using the cloud thickness is to calculate the mass loading in kg m^{-2}, that is, a column loading– this approach circumvents the need to derive the plume thickness.

Table 3.1: Retrieved mass loadings and mode radii for the two size distributions used and for four Ruapehu plumes. The range of mass loadings shown corresponds to a range in cloud thickness from 1.5 km to 3.0 km.

Date:Time	Sensor	Size distribution			
		Log-normal		Modified–γ	
		Mass loading (mg m^{-3})	Mode radius (μm)	Mass loading (mg m^{-3})	Mode radius (μm)
17-06-96:1506	AVHRR-2	3.5–6.9	2.7	3.2–6.3	2.7
08-07-96:1040	ATSR-2	1.4–2.7	3.1	1.4–2.6	3.1
08-07-96:1440	AVHRR-2	1.5–2.9	3.0	1.4–2.6	2.9
08-07-96:1909	AVHRR-2	1.7–3.2	3.2	1.5–2.9	3.5

The retrievals for the 8 July Ruapehu plumes plumes should be comparable, as the time difference between the AVHRR-2 and ATSR-2 data acquisitions is not long (less than five hours) and the eruptions during these days were similar in nature. The mode radii on all days are similar, but the mass loading differences between the June eruption and the July events are probably significant.

Hobbs *et al.* (1981) made aircraft-based measurements of the size distributions and number densities of ash in the periphery of the Mt. St. Helens plume. Some measurements were made at 3 km altitude and 9.3 km downwind of the volcano and these can be compared with our results. For particles in the size range 1–5 μm, the number density is of the order 10–1 cm^{-3} (see Fig. 2B of Hobbs *et al.*, 1981), which correspond to mass loadings of 0.1–1.0 mg m^{-3}. Sehmel (1982) also reported mass loadings in the range 1–10 mg m^{-3} in the dispersed Mt. St. Helens volcanic cloud. Our results may also be compared with silicate mass loading retrievals by Yu and Rose (1999) for the El Chichón clouds, and from recent estimates made by W. I. Rose for the June - September 1992 Spurr eruptions (personal communication). These mass loadings were found to be in the range 1–5 mg m^{-3}. Wen and Rose (1994) determined the total mass of fine particles for the August 19 1992 Crater Peak/Spurr eruption and obtained a value of 0.2 x 10^6 t. They estimated the cloud area to be 10^5 km^2, giving a mass loading range of 1.5–3.0 mg m^{-3} for a cloud thickness range of 1.5–3.0 km. Wen and Rose also show that their total mass estimates are not significantly affected by the choice of size distribution.

The mean retrieved mass loadings are an order of magnitude smaller than the value considered hazardous to aircraft (cf. $\approx$ 50 mg m^{-3} or greater). The mass loadings calculated here represent only those particles in the restricted size range, $1 < r < 8$ μm, and these represent only a small fraction

of the total mass of ejected matter. However, these are the particles which are most hazardous to jet engines and it would appear to be necessary to develop a mass loading threshold based on particles in this size range. The mass in this size range typically represents $\approx 1\%$ of the total mass ejected (e.g. Wen and Rose, 1994; Bursik *et al.*, 1994), which suggests a *total* mass loading of 100–500 mg m^{-3} for the Ruapehu clouds and thus they would have been a threat to jet aircraft.

3.4 Volcanic ash mode–VAM

The new (e.g. MODIS) and proposed advanced multispectral sensors (e.g. GLI, SEVIRI) include many channels capable of providing detection and discrimination of volcanic ash clouds. A model of an ash cloud has been developed in order to exploit these new sensors. We include information from the visible to infrared–although most of the discussion has centred on the infrared window radiances, it seems likely that the visible and near infrared data may also provide a means for ash cloud detection.

At near infrared wavelengths (e.g. λ=1.61 μm) ice clouds appear much darker than clouds of water droplets, because the imaginary part of the refractive index of ice is larger than that of water at this wavelength and consequently ice absorbs more strongly at this wavelength. A comparison of the refractive indices of water, ice and andesite (a common constituent of ash clouds) is given in Table 3.2. Pollack *et al.* (1973) list refractive indices of andesite (and some other minerals) over a large range of

Table 3.2: Refractive indices for water, ice and andesite (a silica-rich mineral). The last column gives the reference to the origin of the data shown.

Wavelength (μm)	n_r	n_i	Reference
Ice			
0.63	1.309	1.04E-8	Masuda and Takashima (1990)
1.61	1.289	3.41E-4	Masuda and Takashima (1990)
Water			
0.63	1.332	1.44E-8	Masuda and Takashima (1990)
1.61	1.317	0.87E-4	Masuda and Takashima (1990)
Andesite			
0.68	1.470	1.70E-3	Pollack *et al.* (1973)
1.61	1.470	3.30E-3	Pollack *et al.* (1973)

wavelengths from the UV to the infrared. These data are not the only source of refractive index values for minerals; see for example, Volz (1973), Ivlev and Popova (1973) and Sokolik and Toon (1999). We have used the Pollack *et al.* (1973) values as a starting point to provide the input optical parameters required for more detailed radiative transfer calculations, and we propose a model of a volcanic ash cloud based on the Pollack *et al.* refractive indices of andesite. The ash cloud model consists of spherical andesite particles in a log-normal size distribution with a mean particle radius of 3 μm. The single-scatter albedo, asymmetry parameter and coefficients of absorption, scattering and extinction are calculated for the polydisperse particle size distribution using the Mie program discussed earlier.

Table 3.3 provides a listing of the the variation of single-scatter albedo (ϖ), extinction coefficient (Q_{ext}), and asymmetry parameter (g) for wavelengths ranging from 0.3 μm to 14.5 μm−the range most commonly used in remote sensing of the earth's atmosphere. Also, shown are the results for a model ash cloud with mean particle radii of 1 and 5 μm.

Table 3.3: Optical parameters for a model andesite ash cloud. The parameters are: ϖ–the single-scatter albedo, g– the asymmetry parameter, and Q_{ext}–the extinction efficiency factor. These parameters are given for three mean particle sizes, r_o=1, 3 and 5 μm.

	r_o=1.0 μm			r_o=3.0 μm			r_o=5.0 μm		
Wavelength (μm)	ϖ	g	Q_{ext}	ϖ	g	Q_{ext}	ϖ	g	Q_{ext}
0.30	0.8346	0.4579	2.0875	0.8344	0.4573	2.0873	0.8343	0.4570	2.0872
0.32	0.8241	0.4551	2.0875	0.8238	0.4543	2.0873	0.8237	0.4540	2.0872
0.34	0.8229	0.4548	2.0876	0.8225	0.4540	2.0873	0.8224	0.4536	2.0872
0.36	0.8104	0.4513	2.0876	0.8100	0.4503	2.0873	0.8098	0.4499	2.0872
0.38	0.8105	0.4515	2.0877	0.8100	0.4504	2.0873	0.8098	0.4499	2.0872
0.40	0.7987	0.4480	2.0877	0.7982	0.4467	2.0873	0.7980	0.4462	2.0872
0.42	0.7988	0.4482	2.0878	0.7982	0.4469	2.0874	0.7980	0.4462	2.0872
0.44	0.7877	0.4448	2.0879	0.7871	0.4433	2.0874	0.7868	0.4426	2.0872
0.46	0.7878	0.4451	2.0880	0.7871	0.4434	2.0874	0.7868	0.4427	2.0872
0.48	0.7879	0.4454	2.0880	0.7872	0.4436	2.0875	0.7868	0.4428	2.0872
0.50	0.7775	0.4421	2.0881	0.7766	0.4401	2.0875	0.7762	0.4392	2.0872
0.52	0.7776	0.4424	2.0882	0.7767	0.4403	2.0876	0.7763	0.4393	2.0872
0.54	0.7778	0.4428	2.0883	0.7768	0.4405	2.0876	0.7763	0.4394	2.0873
0.56	0.7679	0.4396	2.0884	0.7668	0.4371	2.0876	0.7663	0.4359	2.0873
0.58	0.7681	0.4400	2.0886	0.7669	0.4373	2.0877	0.7663	0.4361	2.0873
0.60	0.7683	0.4405	2.0887	0.7670	0.4376	2.0878	0.7664	0.4362	2.0874
0.70	0.7509	0.4363	2.0894	0.7490	0.4321	2.0881	0.7482	0.4302	2.0875
0.80	0.7357	0.4331	2.0903	0.7331	0.4274	2.0886	0.7320	0.4248	2.0878
0.90	0.7225	0.4313	2.0914	0.7191	0.4236	2.0892	0.7176	0.4202	2.0882
1.00	0.7112	0.4308	2.0928	0.7067	0.4209	2.0899	0.7048	0.4165	2.0887
1.10	0.7016	0.4319	2.0945	0.6960	0.4192	2.0908	0.6935	0.4136	2.0892
1.20	0.6937	0.4346	2.0966	0.6866	0.4186	2.0918	0.6836	0.4118	2.0899
1.30	0.6873	0.4392	2.0991	0.6786	0.4193	2.0931	0.6749	0.4109	2.0908
1.40	0.6871	0.4476	2.1021	0.6763	0.4234	2.0945	0.6720	0.4132	2.0917
1.50	0.6834	0.4562	2.1057	0.6702	0.4266	2.0963	0.6651	0.4144	2.0929
1.60	0.6853	0.4685	2.1101	0.6694	0.4331	2.0983	0.6632	0.4185	2.0942
1.70	0.6883	0.4830	2.1155	0.6691	0.4408	2.1007	0.6619	0.4236	2.0957
1.80	0.6926	0.4998	2.1219	0.6695	0.4499	2.1034	0.6610	0.4298	2.0975
1.90	0.6983	0.5189	2.1298	0.6706	0.4605	2.1066	0.6607	0.4371	2.0995
2.00	0.7019	0.5411	2.1395	0.6688	0.4728	2.1104	0.6572	0.4454	2.1019
2.10	0.7143	0.5655	2.1511	0.6749	0.4880	2.1148	0.6614	0.4565	2.1046
2.20	0.7248	0.5909	2.1651	0.6785	0.5038	2.1199	0.6627	0.4677	2.1076
2.30	0.7369	0.6174	2.1817	0.6829	0.5213	2.1258	0.6647	0.4803	2.1110
2.40	0.7507	0.6441	2.2014	0.6882	0.5406	2.1326	0.6672	0.4944	2.1150
2.50	0.7686	0.6699	2.2242	0.6977	0.5621	2.1404	0.6736	0.5109	2.1195
2.55	0.7750	0.6821	2.2369	0.6996	0.5727	2.1448	0.6739	0.5188	2.1219
2.60	0.7845	0.6935	2.2503	0.7049	0.5843	2.1494	0.6775	0.5279	2.1245
2.65	0.7885	0.7045	2.2645	0.7043	0.5953	2.1544	0.6752	0.5361	2.1273
2.70	0.7955	0.7145	2.2795	0.7072	0.6070	2.1597	0.6762	0.5453	2.1302
2.75	0.7931	0.7249	2.2949	0.6996	0.6183	2.1653	0.6670	0.5533	2.1333
2.80	0.7961	0.7338	2.3110	0.6983	0.6306	2.1712	0.6639	0.5630	2.1366
2.85	0.8037	0.7407	2.3277	0.7022	0.6432	2.1776	0.6659	0.5738	2.1401
2.90	0.8091	0.7468	2.3448	0.7040	0.6559	2.1843	0.6658	0.5847	2.1437
2.95	0.8185	0.7507	2.3623	0.7106	0.6682	2.1914	0.6703	0.5963	2.1476
3.00	0.8275	0.7534	2.3800	0.7173	0.6802	2.1988	0.6750	0.6080	2.1517

	r_o=1.0 μm			r_o=3.0 μm			r_o=5.0 μm		
Wavelength (μm)	ϖ	g	Q_{ext}	ϖ	g	Q_{ext}	ϖ	g	Q_{ext}
3.05	0.8381	0.7545	2.3980	0.7265	0.6917	2.2067	0.6821	0.6198	2.1560
3.10	0.8464	0.7549	2.4158	0.7334	0.7028	2.2149	0.6871	0.6316	2.1605
3.15	0.8543	0.7544	2.4335	0.7404	0.7133	2.2235	0.6923	0.6433	2.1653
3.20	0.8635	0.7526	2.4511	0.7498	0.7229	2.2324	0.7000	0.6550	2.1702
3.25	0.8688	0.7511	2.4682	0.7546	0.7325	2.2416	0.7030	0.6666	2.1754
3.30	0.8739	0.7489	2.4848	0.7593	0.7414	2.2512	0.7062	0.6781	2.1807
3.35	0.8803	0.7458	2.5009	0.7664	0.7491	2.2611	0.7118	0.6892	2.1863
3.40	0.8862	0.7423	2.5163	0.7733	0.7560	2.2713	0.7174	0.7000	2.1920
3.45	0.8904	0.7390	2.5308	0.7779	0.7625	2.2817	0.7208	0.7107	2.1980
3.50	0.8943	0.7355	2.5444	0.7825	0.7682	2.2924	0.7242	0.7210	2.2041
3.60	0.9014	0.7281	2.5686	0.7915	0.7773	2.3146	0.7312	0.7403	2.2168
3.70	0.9101	0.7198	2.5882	0.8041	0.7821	2.3376	0.7427	0.7565	2.2302
3.80	0.9166	0.7120	2.6023	0.8140	0.7846	2.3614	0.7518	0.7706	2.2442
3.90	0.9233	0.7042	2.6105	0.8252	0.7842	2.3859	0.7628	0.7815	2.2586
4.00	0.9277	0.7108	2.5773	0.8341	0.7921	2.4195	0.7706	0.7975	2.2773
4.25	0.9352	0.6941	2.5293	0.8494	0.7846	2.4868	0.7858	0.8109	2.3174
4.50	0.9402	0.6765	2.4326	0.8623	0.7737	2.5565	0.7991	0.8122	2.3595
4.75	0.9432	0.6564	2.2915	0.8733	0.7630	2.6272	0.8107	0.8060	2.4037
5.00	0.9413	0.6419	1.9900	0.8819	0.7704	2.6963	0.8184	0.8058	2.4602
5.25	0.9389	0.6130	1.7826	0.8875	0.7668	2.7580	0.8242	0.7977	2.5105
5.50	0.9363	0.5811	1.5711	0.8942	0.7646	2.8121	0.8322	0.7894	2.5637
5.75	0.9300	0.5473	1.3668	0.8966	0.7648	2.8536	0.8351	0.7841	2.6194
6.00	0.9101	0.5133	0.9693	0.9004	0.7970	2.7883	0.8464	0.8093	2.7209
6.50	0.8380	0.4382	0.5776	0.8790	0.8161	2.5113	0.8356	0.8449	2.8205
7.00	0.6549	0.3645	0.3470	0.8058	0.8202	1.9370	0.7889	0.8848	2.6700
7.50	0.3096	0.2950	0.2404	0.5937	0.8105	1.1636	0.6491	0.9068	1.9243
8.00	0.0625	0.2346	0.2882	0.2155	0.7863	0.8026	0.3052	0.9043	1.1673
8.25	0.0655	0.2090	0.4060	0.2279	0.7644	0.9701	0.3203	0.8907	1.3045
8.50	0.1075	0.1876	0.6204	0.3284	0.7318	1.3266	0.4219	0.8611	1.6615
8.75	0.1541	0.1706	1.0082	0.4087	0.6886	1.7910	0.4909	0.8110	2.0317
9.00	0.2049	0.1552	1.7692	0.4686	0.6440	2.3946	0.5405	0.7500	2.4372
9.50	0.1948	0.1366	1.7248	0.4238	0.6592	2.5902	0.4845	0.7775	2.5805
10.00	0.2305	0.1146	1.7813	0.4522	0.6202	2.8094	0.5021	0.7457	2.7180
10.50	0.2495	0.1181	1.3480	0.4546	0.6133	2.8707	0.4883	0.7495	2.7459
11.00	0.3553	0.1286	0.8027	0.5088	0.5991	3.1600	0.4782	0.7452	2.8292
11.50	0.4019	0.0997	0.4043	0.6265	0.5784	3.2195	0.5362	0.7079	3.0643
12.00	0.3958	0.0778	0.2422	0.6997	0.5613	2.8904	0.6367	0.6834	3.3369
12.50	0.3572	0.0625	0.1627	0.7302	0.5433	2.4190	0.7080	0.6870	3.4567
13.00	0.2762	0.0515	0.1285	0.7139	0.5216	1.9619	0.7268	0.7007	3.3357
13.50	0.1904	0.0433	0.1110	0.6736	0.4931	1.5435	0.7210	0.7084	3.0193
14.00	0.1153	0.0377	0.1134	0.5966	0.4607	1.2558	0.6783	0.7107	2.6238

Chapter 4

Product Definitions

We are proposing to supply two base products–ash related maps (particle size, mass, optical depth) and SO_2 related products (SO_2 abundance). These are based on mature algorithms and there will be little research needed but some implementation, testing and validation activities. The definitions of these products are given in the WP description tables and further detail can be found in the earlier text of this ATBD and in the source references. All of the algorithms are based on open source software.

4.1 Naming convention

The naming convention for this product will be:

DateTime+_3-letter Instrument abbreviation+_BTD_IR+_map

The 3-letter abbreviation codes are:

AVH=AVHRR
MOD=MODIS
ATS=(A)ATSR (or ATSR, ATSR-2 for retrospective studies)
SEV=SEVIRI
AIR=AIRS
IAS=IASI
GOE=GOES
MTS=MTSAT

The *DateTime* will be of the form:

dd_mm_yyyy_hr_mn

where dd=day of month (1–31), mm=month of year (1-12) and yyyy=4-digit year. The time will be UTC: hr=hours (0–23) and mn=minutes of hour (0:59). The time will be taken from the time

stamp of the raw data and will usually pertain to the start of the image or granule.

4.2 Product formats

Product formats will conform to industry standards wherever possible. It is planned that binary data files will be stored in HDF or netCDF formats. Most products will be distributed via a web-based tool and in a graphical, image-type format as requested by users in responses to the SAVAA questionnaire. Thus the principal format will be of image type (JPEG, GIF, TIFF or PNG – all 4 formats will be supported but preference will be given to JPEG). A short TEXT file will accompany each image, providing at the minimum the following entries:

1. Event descriptor (a sequence code used for internal auditing)
2. Date of image
3. Time of image (UTC; hrs:mins)
4. Instrument used
5. Product name
6. Generation date/time/software version
7. Brief description of image

As it is possible that many products will be generated for a given event, the intention is to keep the TEXT file information to a minimum. An internal data-base will be maintained with more detailed information about each product generated. The Event Descriptor will be used to identify products with the database.

4.3 Product delivery mechanisms

Products will be delivered in accordance with the wishes of users and will initially be based on the feedback provided in the SAVAA Users Questionnaire. The main delivery mechanism will be via the VAS^3 system, which will be a web-based "click-to-download" system. ftp pull transfers will also be supported. A limited archive of data will be available for download, but this will be purged from time to time to free up disk space. Data off-loaded from the server will be maintained in archive and available to users upon request.

Chapter 5

Validation plan

5.1 Principles

Validation of the ash products is extremely difficult because there are very few independent measurements of ash properties available. The main techniques for measuring ash rely on infrared data and may not be considered as completely independent. Nevertheless it is possible to devise a validation plan that encompasses all the main data sources and methodologies capable of providing information on ash properties. Thus models of dispersion and ashfall can be used to constrain mass limits and the spatial spread. Likewise, in some locales (e.g. Etna) there is infrastructure available to do some field measurements of ash on the ground and use visual observations form ground-based observers.

5.2 Cross validation between instruments

The main consistency check for the ash products will be a cross-validation exercise between the same product from different sensors. The normalized ash map products can be compared after allowing for any mismatches in time. The SEVIRI data, with 15 minute sampling interval will be a useful guide for determining the size of temporal mismatches. All other ash products (ash mass, particle size and optical depth) can also be compared in this way. Since the purpose of the cross-validation is not to determine the correct value, but rather to assess consistency, statistical measures will be used. Three measures will be calculated:

1. σ_e – The standard deviation of the product from the mean of all instruments used
2. Σ_e – Bias of the mean of each product from the mean of all instrument used
3. NΔ_i – Product noise figures based on the instruments' noise equivalent brightness temperature difference (NEΔT)

The first two measures will give the user an idea of the variability of the products with regard to the particular event, while the third measure provides an assessment of the intrinsic noise associated with

measurements from different instruments. Product noise is calculated according to:

$$N\Delta_i = \sqrt{NE\Delta T_{i,11}^2 + NE\Delta T_{i,12}^2}, \tag{5.1}$$

where:

$$NE\Delta T_{i,\lambda} = \sigma_{i,\lambda} \left(\frac{\partial B[\lambda, T]}{\partial T} \right)^{-1}_{i,T_c},$$

B is the Planck function,
T_c is the ash cloud temperature evaluated as the mean of $T_c(11)$ and $T_c(12)$,
λ is the wavelength (11 μm or 12 μm),
i denotes instrument (e.g. AVHRR, MODIS, SEVIRI, (A)ATSR),
$\sigma_{i,\lambda}$ is the nominal noise figure (in radiance) at 280 K for instrument i at wavelength λ.

5.3 Validation with models

The FLEXPART particle dispersion model (Stohl *et al.*, 1988) will be used to analyze the spatial and temporal distribution of ash for specific case studies. These data can be compared with the ash maps and to a limited extent with the geophysical ash products (mass and particle size). Since model errors are also present it will not be possible to unambiguously determine the retrieval errors. Comparison of the model outputs can be done against other dispersion models (e.g. HYSPLIT) giving some idea of the likelihood and size of model error compared with satellite retrieval error.

5.4 Validation with ground-based data

INGV operate a number of observatories near to active volcanoes. Etna is one such volcano and is an obvious choice for detailed intercomparisons. Visual observations, spectrophotometer and other ground-based data (e.g. DOAS and UV spectrometer, and imaging cameras) will be used as available. In the time-frame of the SAVAA project (2009–2011), at least two detailed comparisons with ground-based data will be attempted. Radar data may also be useful for examining the vertical and horizontal extent of ash clouds during the early stages of evolution.

5.5 Validation with *in situ* measurements

Very limited *in situ* data are available for ash validation. Probably the best source of data will be from aircraft campaign measurements or possibly from Unmanned Aerial Vehicle (UAV) missions. The SAVAA team is actively investigating collaborations with groups capable of making *in situ* measurements, especially from UAVs. Other types of *is situ* data include ashfall data–samples collected from the field following a recent eruption. These data could be valuable for determining the spatial extent and distribution of ash.

5.6 Comparisons with other methodologies

There are now some sophisticated models available for simulating the fall, and subsequent distribution of ash on the ground. Simulated ashfall maps may be compared with ash in the air to validate the spatial distribution of ash. It may also be possible to utilise satellite imagery to determine the extent of ash on the ground and relate this to ash in the air. A study of this kind is in progress at NILU.

Chapter 6

Ash Alert

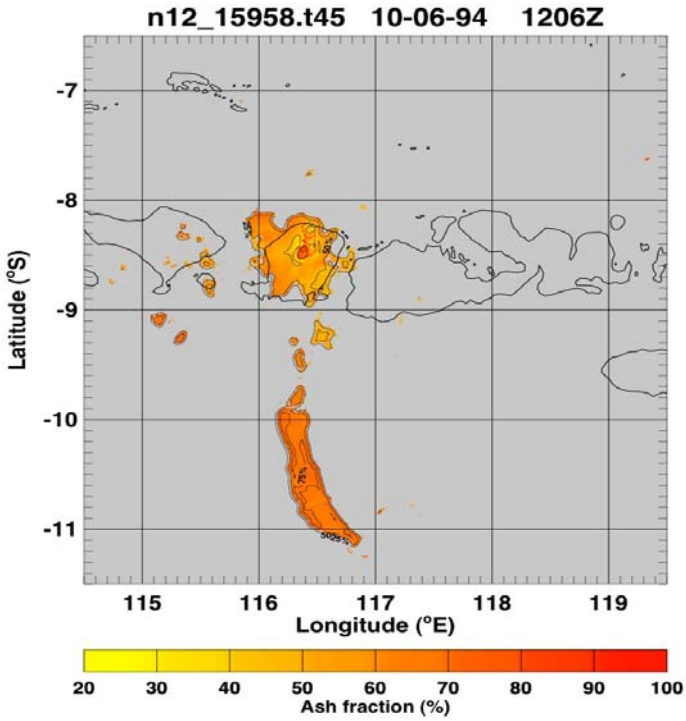

Ash fraction map for the eruption of Rindjani, Indonesia.

6.1 Reverse Absorption Method (RA)

Silica-bearing ash clouds can be discriminated from water/ice clouds by comparing the brightness temperatures in two nearby infrared window channels. The essential feature of this signature is that at wavelengths between 8 and 14 μm, silicate particles absorb infrared radiation more strongly at shorter wavelengths, while water droplets, water vapour and ice particles (the most common constituents of meteorological clouds) absorb more strongly at longer (infrared) wavelengths. Many particulates ejected from vigorous volcanic eruptions have compositions with a high silica (SiO_2) content.

The detection technique consists of deriving brightness temperatures from channels at 10.8 μm and at 11.9 μm), hereafter referred to as T_4 and T_5, and constructing 2-dimensional histograms for cloudy regions. Theoretical analysis (e.g. Prata, 1989b), radiative transfer modelling (e.g. Wen and Rose, 1994) and satellite-based experimental studies (e.g. Prata, 1989a) have shown that for water/ice clouds the difference in brightness temperature between T_4 and T_5 is positive, while for silica-bearing clouds the difference is negative. A plot of T_4-T_5 versus T_4 (or T_5) shows a characteristic arch shape for water/ice clouds (e.g. Parol *et al.*, 1991) and a distorted U-shape for silica-bearing (ash) clouds. Thus a discriminant for ash clouds is

$$T_4 - T_5 < T_{cut-off}. \tag{6.1}$$

In ideal circumstances $T_{cut-off}$ should be 0 K, but because of calibration uncertainties, field-of-view misalignment and mixed pixel effects, the value of $T_{cut-off}$ is chosen to be in the range -0.5 K to $+0.5$ K. Figures 6.1(a)-(c) show a sequence of multispectral daytime images of the Mt Ruapehu plume discriminated using condition (6.1) with $T_{cut-off}$=0.5 K, overlayed with a false-colour enhancement using the visible channels (1 and 2 for AVHRR-2 and the 0.67 μm and 0.87 μm channels in the case of the (A)ATSR, MODIS or SEVIRI). All pixels in the images were tested using condition (6.1); those that passed the condition were assigned a red-to-yellow colour based on the pixel's exact value of T_4-T_5 (the reddest pixels correspond to the most negative differences). Figure **??**(d) shows a nighttime AVHRR-2 image showing an ash plume also discriminated using condition (1), but with a cut-off of $+0.25$ K. The higher value of the cut-off is chosen because experience has shown that at night over cloud-free land $T_4 - T_5$ can be slightly negative. The yellow-coloured regions on land to the north-west of the main plume are regions of cloud-free land. This analysis indicates which clouds are silica-bearing and which are not. At the edges of the (discriminated) ash cloud there is likely to be significant mixing with ambient air which, in all likelihood, contains water vapour and/or water droplets. Therefore at the edges it is probable that pixels contain both ash and water droplets in varying amounts leading to misidentification. Thus the precise identification of the edge of the plume will always be problematic using this technique and from a safety point of view the location of the ash cloud boundary should be treated with large uncertainty. In the most opaque parts of the cloud, the temperature differences tend to 0 K as the cloud starts to behave as a grey-body. This behaviour excludes the possibility of unambiguous identification of silicate particles.

Similar comments can be made about the use of the thermal channels of the (A)ATSR, MODIS and SEVIRI as condition (6.1) is largely insensitive to the precise position of the bands (within the 10-12 μm window), and only slightly sensitive to the bandwidths and band overlap between channels. There is a much greater sensitivity to the noise characteristics of the channels and to their digitisation. Noise becomes a particularly serious problem at low ash cloud loadings because the discriminator relies on the difference between two measurements.

6.1.1 Theoretical basis

In highly simplified form, the theoretical basis for the reverse absorption method can be demonstrated by the following argument. Suppose that the radiances can be linearised to brightness temperatures and that at the satellite these quantities have the values, T_4 and T_5 for channels situated at approximately 11 μm and 12 μm, resepectively. Suppose also that the cloud top has a temperature T_c, that the cloud is semi-transparent and that the surface below behaves as a blackbody radiator with temperature T_s, $T_s > T_c$. Denoting the emissivities of the cloud at 11 μm and 12 μm as ϵ_4 and ϵ_5, resepectively, we may write,

$$T_4 = \epsilon_4 T_c + (1 - \epsilon_4) T_s, \tag{6.2}$$

$$T_5 = \epsilon_5 T_c + (1 - \epsilon_5) T_s. \tag{6.3}$$

Assuming that scattering effects of the cloud particles are negligible, then,

$$\epsilon_i = 1 - \exp(-k_i L), \tag{6.4}$$

where k_i is the absorption coefficient for channel i, and L is the geometric thickness of the cloud. Manipulating these equations and setting,

$$\beta = \frac{k_5}{k_4},$$

we obtain,

$$\Delta T = \Delta T_c [X - X^\beta], \tag{6.5}$$

where,

$$X = 1 - \frac{\Delta T_4}{\Delta T_c},$$

$$\Delta T = T_4 - T_5, \quad \Delta T_c = T_s - T_c, \quad \Delta T_4 = T_s - T_4.$$

It is instructive to examine (6.5) for the cases when $\beta < 1$, $\beta > 1$, and $\beta = 1$. It can be seen that the cases $\beta < 1$ and $\beta > 1$ lead to opposite curvatures.

This result is the basis for discriminating volcanic ash clouds from water/ice clouds by utilising a plot of the temperature difference between AVHRR-2[1] channels 4 and 5 against AVHRR-2 channel 4 temperature. This plot is a 2-dimensional histogram for the set of discrete measurements made from a satellite instrument such as the AVHRR-2. MODIS, SEVIRI or (A)ATSR. For ash clouds, the absorption coefficient at 11 μm is less than that at 12 μm, while the opposite is the case for water/ice clouds. This simple analysis also shows that for clouds with a low temperature contrast ($\Delta T_c \approx 0$), discrimination from the shape of the curve is difficult or impossible. A more complete analysis shows that it is the ratio of extinction coefficients (absorption and scattering) that determines the shape of the curve.

[1]Here and onwards when we refer to AVHRR-2 channels, the remarks have equal validity for equivalent MODIS, SEVIRI, or (A)ATSR channels.

6.1.2 Accounting for water vapour

Water vapour has a differential absorption effect on the infrared window radiances so that at the top of the atmosphere the radiance (or brightness temperature) is larger at 11 μm than at 12 μm. This is the opposite to the absorption effect caused by volcanic ash and thus water vapour can 'hide' the ash effect. A method to correct for the water vapour effect, based on global radiative transfer simulations has been devised and is described here.

6.1.2.1 Global radiative transfer calculations

Detailed radiative transfer (RT) calculations were performed using the MODTRAN-3 code to determine the top-of-the-atmosphere (TOA) brightness temperatures for the AVHRR, MODIS, SEVIRI and (A)ATSR split-window channels. The calculations utilised global NCEP analyses for four different days and two different times. The days and times were chosen to represent seasonal and diurnal variations in atmospheric water vapour conditions. Figure 6.2 shows the global distributions of TOA brightness temperature at 11 μm (top panel), the precipitable water amount (cm), and the temperature difference ($T_4 - T_5$) between the 11 μm and 12 μm AVHRR split window channels. The calculations shown are for 26 December 1996 at 00Z. The most notable feature of these calculations is the high degree of spatial correlation between the fields of precipitable water and $T_4 - T_5$. There is a marked nonlinear relationship between the TOA brightness temperature and precipitable water. Similar results were found for the other days and times.

Water vapour amount is not distributed uniformly over the globe. Largest amounts are found in tropical and subtropical regions while the polar regions are relatively dry. Water vapour distributions also appear to follow weather systems and the patterns resemble the cloud patterns associated with frontal systems. There also appears to be a strong correlation between warm ocean current systems and high water vapour loadings. These general patterns in water vapour amount (or precipitable water) are reflected in the global patterns of AVHRR T_4-T_5.

6.1.2.2 A semi-empirical water vapour correction

The RT calculations suggest that there is a very strong correlation between precipitable water and $T_4 - T_5$ and a strong, but nonlinear correlation between precipitable water and top-of-the-atmosphere temperature at 11 μm or 12 μm. This latter nonlinear relation derives from the correlation between SST and precipitable water. Therefore there exists a nonlinear correlation between $T_4 - T_5$ and T_4 through precipitable water. This fact is no surprise as it is the basis for estimating SST from the AVHRR and other instruments relying on the split-window channels.

Figure 6.3 shows the correlations between precipitable water (in cm) and $T_4 - T_5$, and T_4 and $T_4 - T_5$ calculated using RT and the NCEP data described earlier.

The data shown are for 26-12-1996 at 00Z, but very similar results are obtained for other dates and times. Also shown on Figure 6.3 are empirical fits providing upper and lower bounds to the distribution of the points. The semi-empirical relations describing these bounds are,
Upper bound:

$$\Delta T_{wv} = \exp\left[20T_* - 18\right]. \tag{6.6}$$

Lower bound:

$$\Delta T_{wv} = \exp\left[6T_* - b\right], \tag{6.7}$$

where $T_* = T_4/T_{max}$, and T_{max} is an arbitrary normalisation constant assigned a value of 320 K. The free parameter b essentially determines the value of the water vapour effect on $T_4 - T_5$ at the maximum value of T_4. Hence b can be determined directly from the image data, allowing realistic flexibility on the size of the water vapour correction determined by this semi-empirical approach.

6.1.2.3 Test case: Rindjani eruptions, Indonesia, June 1994

The semi-empirical approach to water vapour correction for volcanic ash detection has been tested on some eruptions of Rindjani volcano on the island of Lombok in Indonesia. These eruptions were mostly low level and occurred in a moisture laden, tropical atmosphere. Detection using the reverse absorption effect was successful on many AVHRR images, but it is known from the work of Prata (1989a, b), Wen and Rose (1994), and Davies and Rose (1998) that water vapour will have the effect of suppressing the size of the negative differences. Thus a water vapour correction is warranted. Four test cases are shown in Figure 6.4, where distributions of $T_4 - T_5$ vs. T_4 are plotted without a water vapour correction (black points), and with a water vapour correction (red points).

The continuous line is a simplified model of the behaviour of ΔT for volcanic ash clouds described by Prata and Grant (2001) and developed from radiative transfer considerations. The model may be written:

$$\Delta T = \Delta T_s[X - X^{\beta}], \tag{6.8}$$

where,

$$X = 1 - \frac{\Delta T_s}{\Delta T_4},$$
$$\Delta T_4 = T_4 - T_c,$$
$$\Delta T_s = T_s - T_c,$$

and the cloud-top and surface temperatures are T_c and T_s. The parameter β links the spectral behaviour of the top-of-the atmosphere brightness temperatures (T_4, T_5) to the cloud microphysics, through the ratio of spectral extinction efficiencies for volcanic ash. Mie calculations by Prata (1989b) and Prata and Barton (1994) for silicate spherical particles suggest values of β from ≈ 0.6 to ≈ 0.86. A value of β=0.71 was used in Figure 6.3.

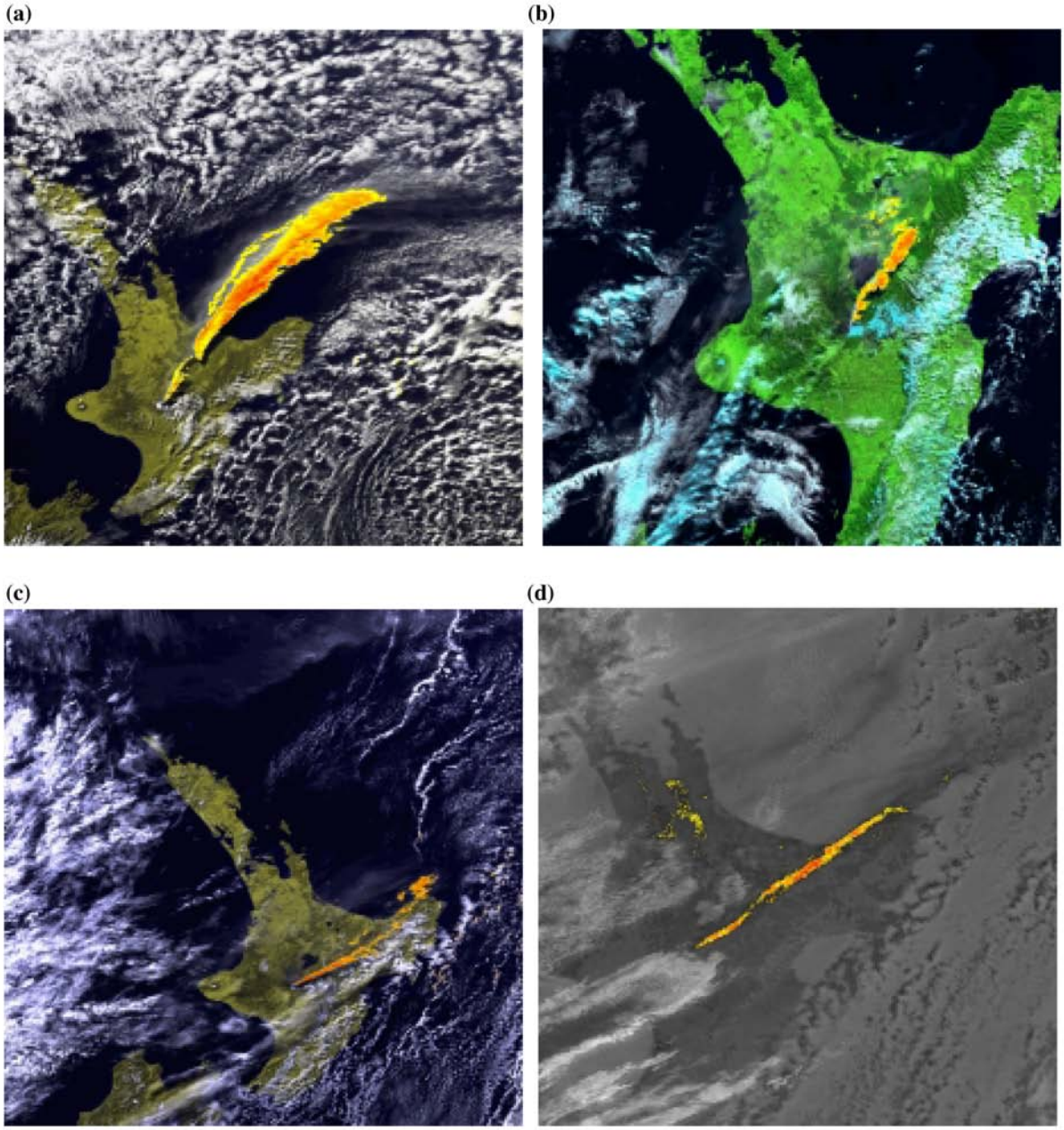

Figure 6.1: (a) Ruapehu plume identified in AVHRR-2 data at 1506LT on 17 June, 1996. (b) Plume identified in ATSR-2 data at 1040LT on 8 July, 1996. (c) Plume identified in AVHRR-2 at 1440LT on 8 July, 1996. (d) Plume identified in AVHRR-2 at 1909LT on 8 July, 1996. Reddest regions correspond to the most negative T (11 μm) - T (12 μm) temperature differences.

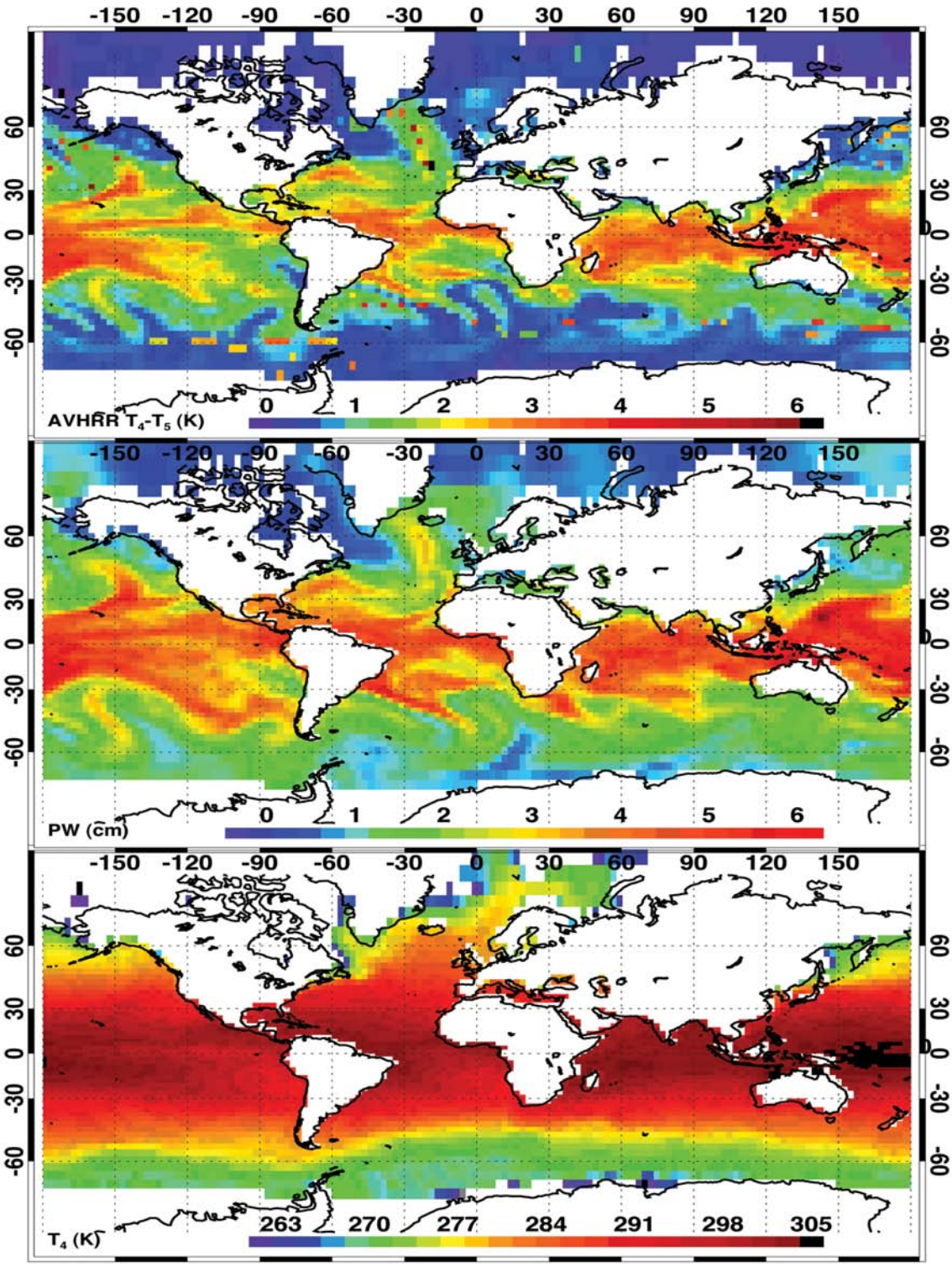

Figure 6.2: Global distributions of 11 μm - 12 μm brightness temperatures (T_4-T_5, K; top panel) precipitable water (cm; middle panel) and 11 μm brightness temperature (K; bottom panel) for 26 December 1996 at 00 Z.

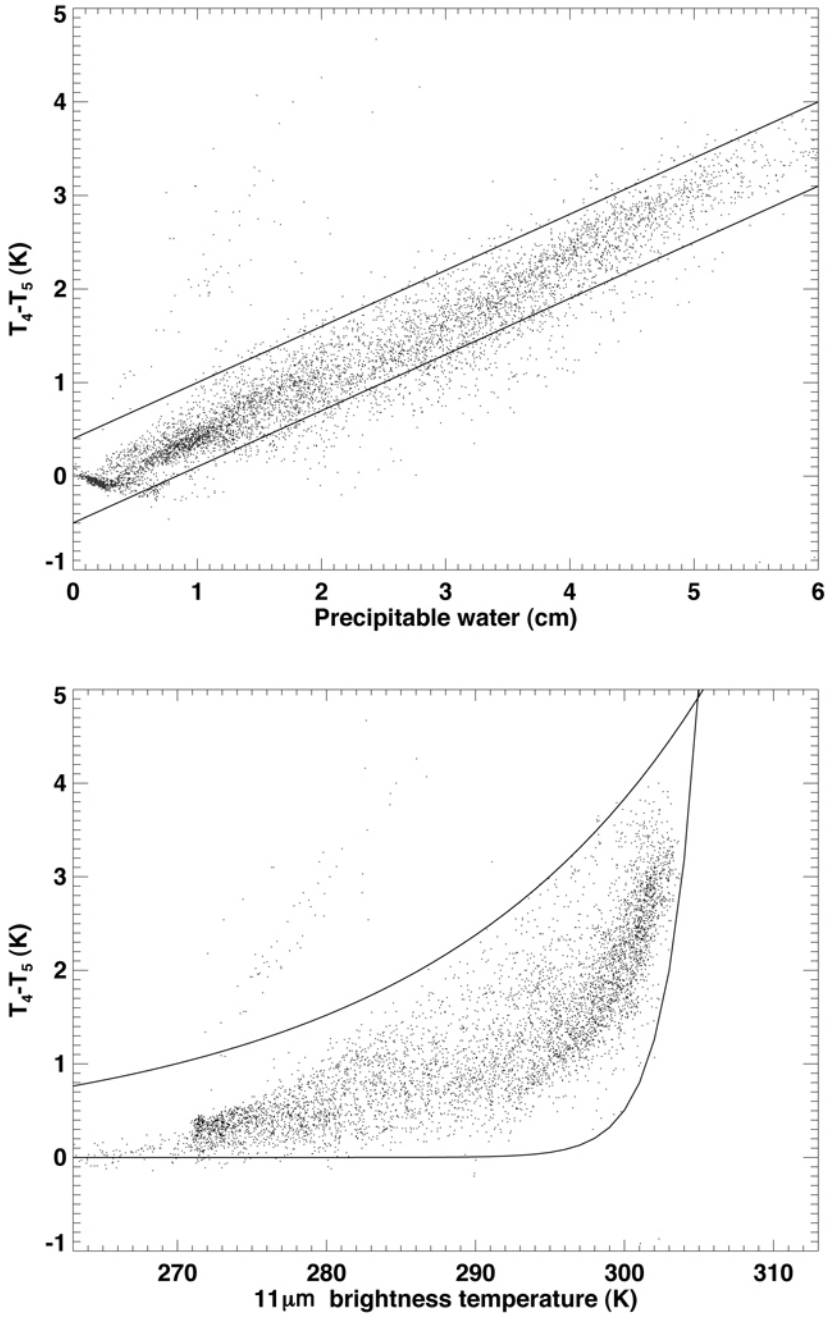

Figure 6.3: Global distributions of 11 μm - 12 μm brightness temperatures (T_4-T_5, K; top panel) precipitable water (cm; middle panel) and 11 μm brightness temperature (K; bottom panel) for 26 December 1996 at 00 Z.

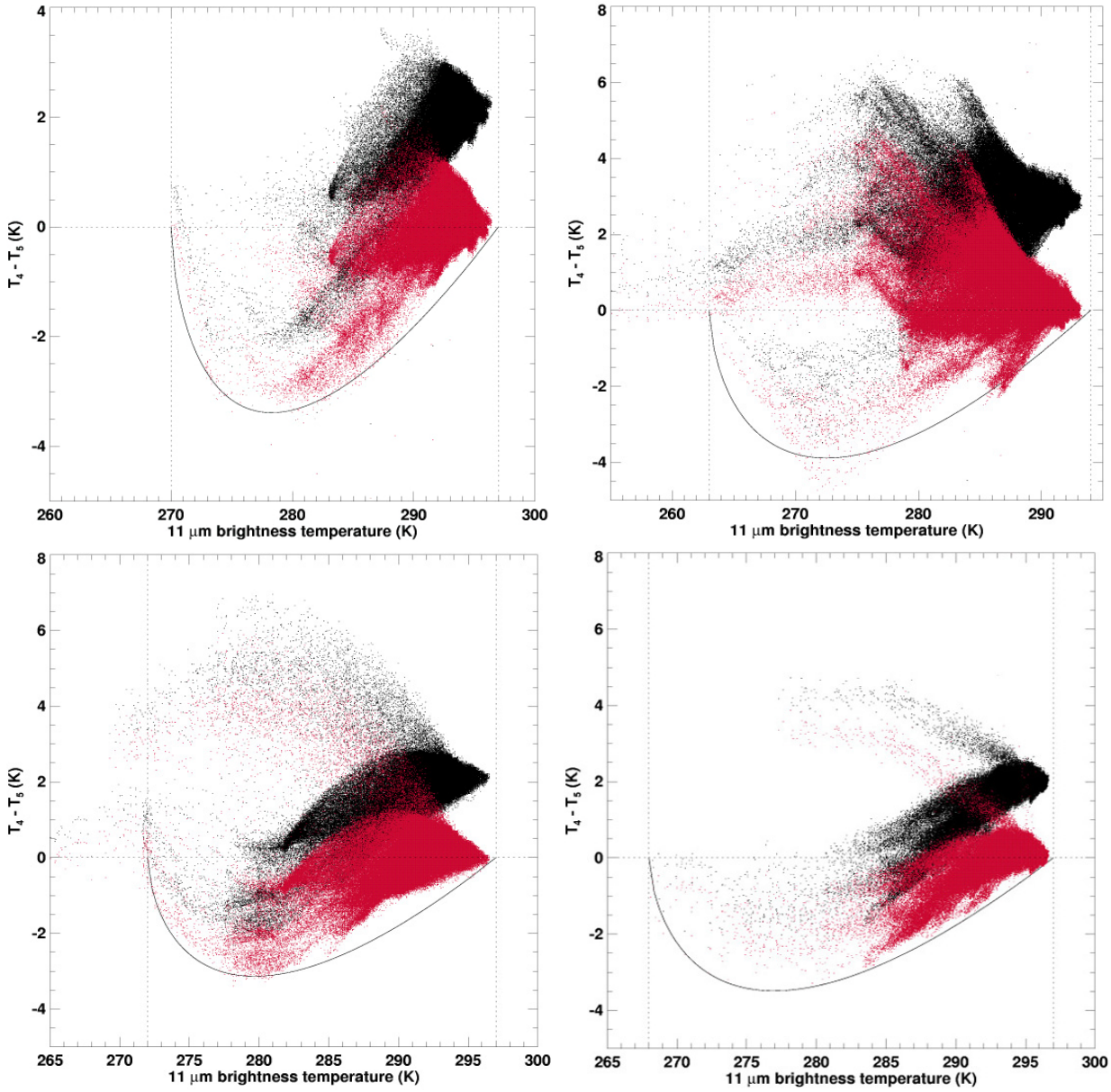

Figure 6.4: Temperature difference distributions without (black dots) and with (red dots) a water vapour correction for four different eruption clouds from Rindjani, Indonesia.

Theory suggests values of $\Delta T < 0$ are ash, but this does not take into account measurement errors, primarily resulting from instrument noise, poor calibration and channel misregistration. The water vapour correction and the theory utilised are also approximations and contain some degree of uncertainty. Each pixel is likely to contain a mixture of water vapour and ash. We assume that the temperature difference observed arises from a linear combination of the signal from ash (ΔT_{ash}) and the signal from an otherwise clear pixel, any temperature difference being due to water vapour (ΔT_{wv}). If the fraction of ash in the mixture is F, then we may write the observed temperature difference as,

$$\Delta T = F \Delta T_s [Z - Z^{\beta}], \tag{6.9}$$

where,

$$Z = 1 - \frac{1}{F} \frac{\Delta T_4}{\Delta T_s},$$

The other parameters are defined as before. Ideally this procedure needs to be automated. There are several parameters that can be determined from the image data. These are:
(1) the clear-sky surface temperature T_s, (2) the cloud-top temperature T_c, (3) the clear-sky value of the water vapour correction, parametrised by b, and (4) the ratio of extinction coefficients β that governs the magnitude of the "U"-shaped distribution of negative differences.

A procedure for estimating these parameters from the image data has been developed. A brief outline is given below.

1. T_s. This is easily estimated by finding the maximum value of T_4 occurring in the data. A component for water vapour absorption correction is added using the method described earlier.

2. T_c. This is more difficult to estimate from the data, because the lowest value may not necessarily correspond to the volcanic cloud. However, provided an area in close proximity to the suspect cloud can be delineated it may be reasonable to assume that the lowest value is the cloud-top temperature.

3. b. This is estimated by evaluating $T_4 - T_5$ for the pixel corresponding to the maximum value of T_4. Then (2) is solved for b. Values of 3 to 5 appear to be acceptable.

4. β. Theoretical estimates of β suggest a value of around 0.7. A method for estimating β, T_s and T_c simultaneously has been developed by using the distribution of T_4 *vs* $T_4 - T_5$. The distribution is first histogrammed (or binned) into intervals of 0.5 K in T_4. Then, the lowest values in each bin are found and a curve is generated giving the outline of the distribution. The curve is smoothed and fitted using a nonlinear least squares model. The model has three parameters, *viz.*: T_s, $T_s - T_c$ and β that can be estimated from the fit.

The curve-fitting procedure uses the model developed earlier with $F = 1$ and the partial derivatives of the model, which are analytic. Writing,

$$Y = \alpha(X - X^{\beta}),$$

where, Y=T_4-T_5, α=T_s-T_c, X=1-$\frac{\gamma}{\alpha}$, γ=T_s-T_4. The partial derivatives are,

$$\frac{\partial Y}{\partial \alpha} = (X - X^{\beta}) + \frac{\gamma}{\alpha} + \beta \frac{\gamma}{\alpha} (1 - \frac{\gamma}{\alpha})^{\beta - 1},$$

$$\frac{\partial Y}{\partial \beta} = \alpha X^{\beta} Log\beta,$$
$$\frac{\partial Y}{\partial \gamma} = 1 - \beta X^{\beta-1}.$$

An example of the curve-fitting procedure is shown in Figure 6.5. The distribution shown is for a volcanic ash plume from the 1996 June eruption of Ruapehu, New Zealand. The solid green-coloured lines are isolines of constant ash fraction F, and the red dots show the extrema of the distribution estimated from the data at constant temperature intervals. The extrema are used as input to (6.9) to determine the parameters of the model for F=1.0. Once these parameters are determined, F can be inferred for all pixels in the distribution.

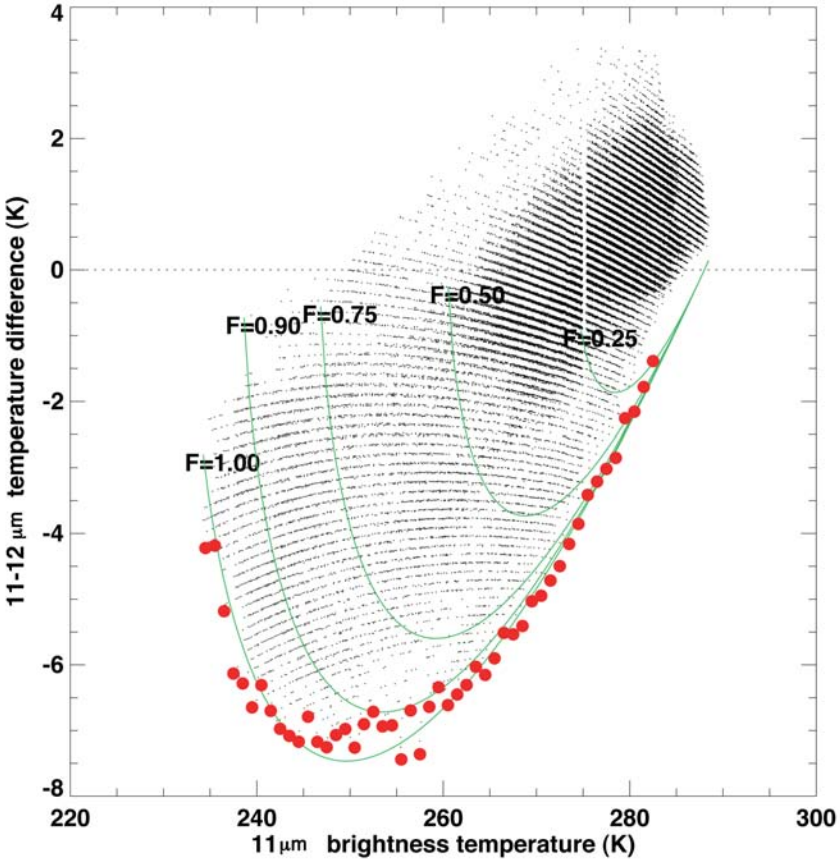

Figure 6.5: Distribution of $T_4 - T_5$ for an eruption of Ruapehu volcano. The green-coloured lines are isolines of the fraction of ash determined from Eq. (6.1). The red dots are estimates of the extrema of the distribution derived from the data.

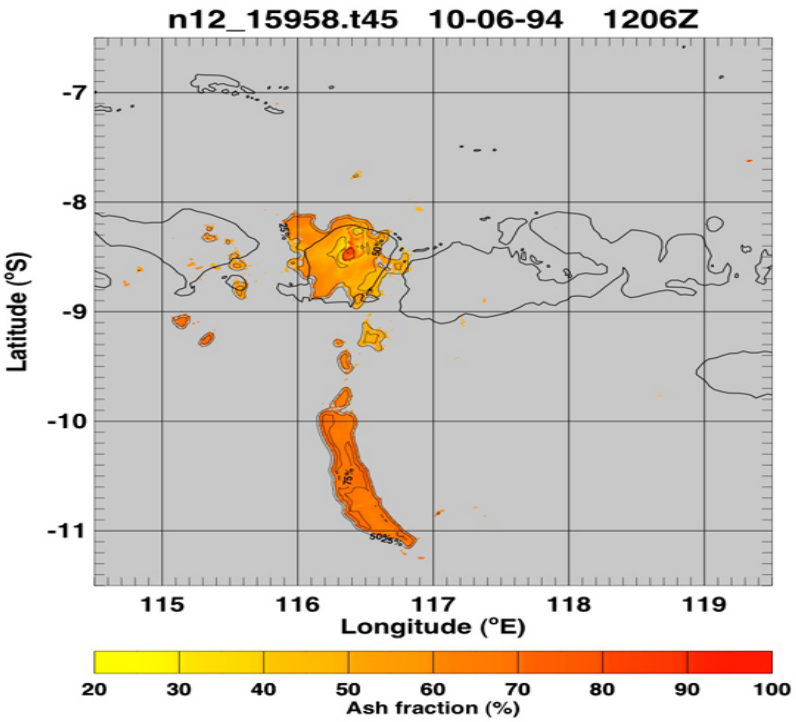

Figure 6.6: Ash fraction retrievals for eruption of Rindjani volcano, Indonesia. The colours and contours show the percentage of ash determined for each AVHRR pixel, assuming that the pixel contains a linear mixture of ash and water vapour components.

The ash fraction maps (Figures 6.6 and 6.7a,b) are an improvement over temperature difference images, but still suffer from ambiguities over land at night due to spectral emissivity effects for land surfaces. These can be overcome using a modified correction scheme that accounts for these emissivity effects over the land. The correction simply allows for a lower emissivity at 11 μm than at 12 μm for pixels identified as land (using a map data-base) and have been applied to the nighttime images. Further improvements are likely by utilising a land cover scheme that identifies land pixels by their vegetation cover.

A similar approach to water vapour correction is described by Yu *et al.* (2002).

6.2 Concavity Algorithm

This algorithm is an extension of the RA and uses high-spectral resolution data from AIRS and IASI. The basic theory behind the Concavity algorithm is described in Gangale *et al.* (2009).

The new algorithm for ash detection is based on the different behaviour of the spectral curves in the wavenumber range between 800 and 1130 cm^{-1}. The shape of these curves depends on both particle size and composition of the observed aerosol and therefore has a physical basis. The main features of

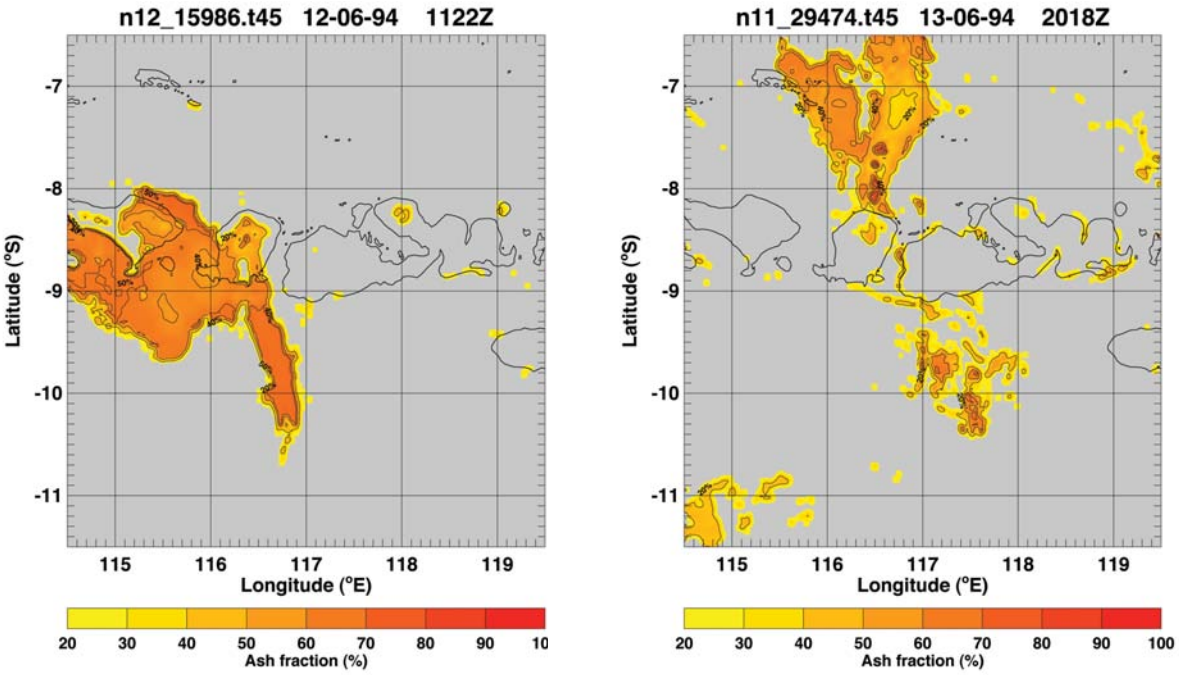

Figure 6.7: As for 6.6, but different times and dates.

these signatures are summarized below:

1. A marked negative concavity of the Chaitén ash curve between 800 and 960 cm^{-1}.
2. The curve has a maximum between 800 and 900 cm^{-1}.
3. There are different slopes of the curves between 910 and 980 cm^{-1}. In particular the signature for the ice cloud has a strong positive slope in this range while for the others it is negative or flat.
4. Different slopes of the curves between 1070 and 1130 cm^{-1}. In particular the ice cloud signature is flat or slightly negative, while the others have positive slopes.

For each pixel of the image, the curves are approximated by a polynomial function in three different intervals. A quadratic function is used to fit the curves between 800 and 960 cm^{-1} and the second degree coefficient is the concavity ($\mathcal{C}$)[2]. The linear Pearson correlation coefficient ($\mathbf{r}$) is calculated in order to have a measure of the goodness of fit. Once the coefficients of the fitting parabola have been calculated, the abscissa of the maximum (ν_{max}) is also computed. Linear fits are used in the 910–980 cm^{-1} and 1070–1130 cm^{-1} intervals and the first degree coefficients are the slopes ($\mathbf{s}_1$ and $\mathbf{s}_2$, both multiplied by a factor 10^4 for convenience). Some wavenumbers have been excluded from the curve fitting because they are affected by water vapour absorption and these could be a source of error in

[2]For convenience $\mathcal{C}$ has been multiplied by a factor 10^6.

the fit. There are many ways to exploit these estimated parameters in order to discriminate volcanic ash from other types of airborne particles and hydrometeors. Here we outline one such scheme that has worked well for some of the ash clouds we have examined; however, we caution that this scheme may not be optimum and a more detailed study using many more case studies and using both AIRS and IASI spectra is planned.

A pixel is assumed to be part of the volcanic plume if all the following conditions are satisfied:

$$\mathcal{C} < 0.0, \mathbf{r} > 0.6, \mathbf{s}_1 < 0.0, \mathbf{s}_2 > 0.0 \quad \text{and} \quad 780\ \text{cm}^{-1} < \nu_{max} < 880\ \text{cm}^{-1} \tag{6.10}$$

It is likely that some tuning of the conditions (6.10) may be required for different ash clouds and possibly different atmospheric conditions. In particular a more robust condition, leading to fewer detections (some possibly false) has been used with $\mathcal{C} < -1.0$. This algorithm has been tested on many AIRS images of ash clouds, but we focus here on those from the Chaitén volcanic eruption, which started on 2 May 2008 (see Carn *at al.*, 2009, for a description of the eruption). Results are compared with the 'reverse' absorption (RA) method, which is done by calculating temperature differences over narrow bands centred near to 830 cm^{-1} and 910 cm^{-1}. Integrating the AIRS radiances over the MODIS filter response functions corresponding to MODIS bands 31 and 32, provides corresponding AIRS narrow band channels.

When the ash cloud becomes opaque the concavity $\mathcal{C}$ tends to zero or can even become positive, while the slope $\mathbf{s_2}$ remains positive. For this reason another set of conditions was developed to assign a pixel that contains volcanic ash,

$$\mathcal{C} > 0.0, \mathbf{r} > 0.6, \mathbf{s}_2 > 1. \tag{6.11}$$

The concavity algorithm produces less noisy images than the RA images, and seems to be quite sensitive to optically thin volcanic clouds. The ash plume detection is similar both over land and over the sea with no discontinuities while the RA method is affected by the thermal contrast between the ash cloud and the surface below, especially when the infrared opacity is small.

Ash detections using the concavity ($\mathcal{C}$) algorithm for the Chaitén eruption starting on 3 May and ending on 7 May show that this method identifies ash 96 hours after the initial eruption and more than 5,000 km from the source. Figure 6.8 shows $\mathcal{C}$ (scaled by a factor 10^6) as coloured points for 19 AIRS granules between 2–7 May, 2008 over a region where the Chaitén ash was transported. Although there are no corroborating data to verify ash detection, HYSPLIT trajectories (also shown in Fig. 6.8 for three different starting altitudes) are consistent with the positions of the $\mathcal{C}$ ash detections. CALIPSO data were examined to look for volcanic aerosols, and two possible detections (shown as inset images in Fig. 6.8) are suggested on 5 May at around 15:15 UT and on 7 May at around 04:50 UT. Carn *et al.*(2009) identified the latter case as an ash cloud. The CALIPSO level 2 browse vertical feature mask product (`http://www-calipso.larc.nasa.gov/products/lidar/browse_images/production/` identifies the feature on 5 May as "stratospheric". However, it is difficult to unambiguously identify the Chaitén volcanic aerosol in the Caliop data; this may be due to the lack of significant SO_2 emissions, which in turn suggests that volcanic sulphate aerosol concentrations would have been low. Because methods for unambiguously identifying volcanic ash in the backscatter returns from the Caliop lidar are currently not well developed, these observations must be teated as tentative.

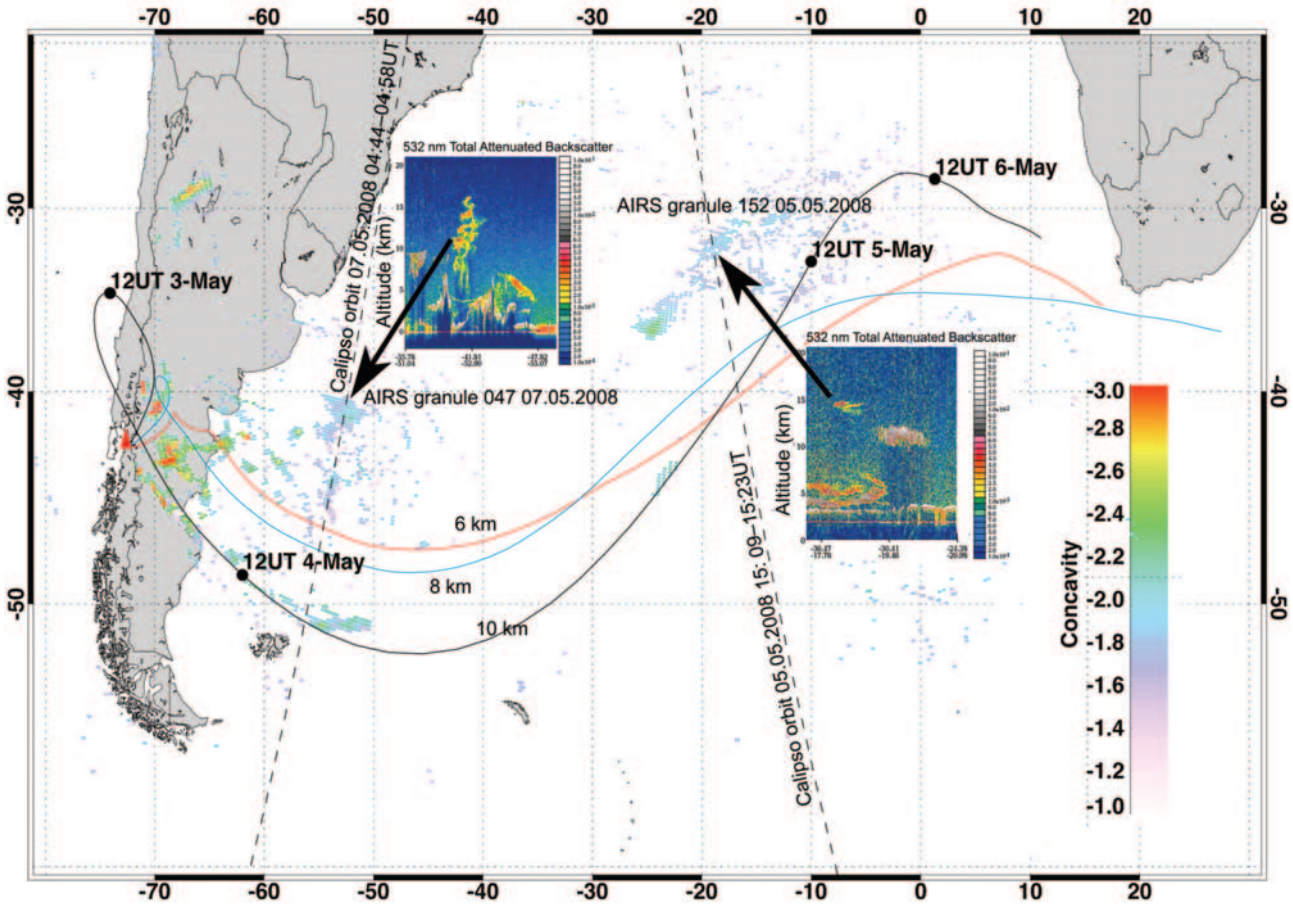

Figure 6.8: AIRS pixels identified as volcanic ash using the concavity algorithm for the Chaitén volcanic eruption of 2 May, 2008. AIRS granules covering the geographic region shown and within the time interval 02.05.2008 18:05UT to 06.05.2008 17:35UT were analysed to calculate $\mathcal{C}$, multiplied by a factor 10^6 and scaled from –3 (red coloured points) to –1 (lilac coloured points). The solid line are HYSPLIT trajectories for air starting at 6, 8 and 10 km asl from Chaitén at 12:00UT, 2 May 2008, and ending 120 hrs later. The dashed lines show two CALIPSO orbits; one on 5 May starting at 15:09 UT and the other on 7 May starting at 04:44 UT. The inset images show cropped portions of the 532 nm total attenuated backscatter (km^{-1} sr^{-1}) from the Caliop lidar on board CALIPSO. The AIRS granules corresponding to the two CALIPSO orbits are also indicated.

6.3 Alert Format

TBD

6.4 Alert Distribution

TBD

Chapter 7

Important literature and references

The following bibliography includes all of the work cited in this ATBD and other reference papers that are relevant to the work of SAVAA. This list may be updated during the lifetime of the project.

Bibliography

[1] Afe, O. T., A. Richter, B. Sierk, F. Wittrock and J. P. Burrows: BrO Emission from Volcanoes - a Survey using GOME and SCIAMACHY Measurements, Geophys. Res.Lett., 31, L24113, doi:10.1029/2004GL020994, 2004.

[2] Barton, I.J., Prata, A.J., Watterson, I.G. and Young, S.A.: Identification of the Mount Hudson volcanic cloud over SE Australia, Geophys. Res. Lett., 19, 1211–1214, 1992.

[3] Berk, A., Bernstein, L. S., and Robertson, D. C.: MODTRAN: A moderate resolution model for LOWTRAN 7, U. S., Air Force Phillips Laboratory, Nascom Air Force Base, MA, U. S. A., **AFGL-TR-89-0122**, 1989.

[4] Bernard, A. and Rose, W. I: The injection of sulfuric acid aerosols in the stratosphere by the El Chichn volcano and its related hazards to the international air traffic, Natural Hazards, 3(1), 59–67, doi:10.1007/BF00144974, 1984.

[5] Bey, I., Jacob, D. J., Yantosca, R. M., Logan, J. A., Field, B. D., et al.: Global modeling of tropospheric chemistry with assimilated meteorology: Model description and evaluation, J. Geophys. Res., 106, 23073–23096, doi:10.1029/2001JD000807, 2001.

[6] Bluth, G. J. S., Schnetzler, C. C., Krueger, A. J., and Walter, L. S.: The contribution of explosive volcanism to global atmospheric sulphur dioxide concentrations, Nature, 366, 327–329, 1993.

[7] Brigss, G. A.: Plume rise predictions. In *Lectures on Air Pollution and Environmental Impact Analyses*, pp. 59–111., American Meteorological Society, Boston, 1975.

[8] Bursik, M. I., Sparks, R. S. J., Carey, S. N., and Gilbert, J. S.: The concentration of ash in volcanic plumes, inferred from dispersal data, *In* Volcanic ash and aviation safety, *Proc. of the First International Symposium on Volcanic Ash and Aviation Safety*, US. Geological Survey Bulletin **2047**, Seattle, Washinghton, July, 1991. 19–29., 1994.

[9] Cadle, R. D., A. L. Lazrus, B. J. Huebert, L. E. Heidt, W. I. Rose, Jr., D. C. Woods, R. L. Chuan, R. E. Stoiber, D. B. Smith and R. A. Zielinski: Atmospheric implications of studies of Central American volcanic eruption clouds, *J. Geophys. Res.*, **84**(C11), 6961–6968, 1979.

[10] Carn, S. A., Krueger, A. J., Krotkov, N. A., and Gray, M. A.: Fire at Iraqi sulfur plant emits SO_2 clouds detected by Earth Probe TOMS, Geophys. Res. Lett., 31, L19105, doi:10.1029/2004GL020719, 2004.

[11] Carn, S. A., Krotkov, N. A., Yang, K., Hoff, R. M., Prata, A. J., Krueger, A. J., Loughlin, S. C., and Levelt, P. F.: Extended observations of volcanic SO_2 and sulphate aerosol in the stratosphere, Atmos. Chem. Phys. Discuss., 7, 2857–2871, 2007.

[12] Carn, S. A., Prata, A. J., and Karlsdottir, S.: Circumpolar transport of a volcanic cloud from Hekla (Iceland), J. Geophys. Res., 2008. (In press).

[13] Carn, S. A., Pallister, J. S., Lara, L., Ewert, J. W., Watt, S., Prata, A. J., Thomas, R. and Villarosa, G.: The re-awenking of Chaitén volcano, *EOS*. **90**(24), 2005–2006, 2009.

[14] Casadevall, T. J.: The 1989/1990 eruption of Redoubt Volcano Alaska: impacts on aircraft operations, J. Volcanol. Geotherm. Res, 62(30), 301–316, 1994.

[15] Casadevall, T. J., Delos Reyes, P. J., and Schneider, D. J.: The 1991 Pinatubo Eruptions and Their Effects on Aircraft Operations. In C.G. Newhall, and R. S. Punongbayan (Eds.), Fire and Mud: eruptions and lahars of Mount Pinatubo, Philippines, 625–636, Quezon City: Philippines Institute of Volcanology and Seismology, Seattle: University of Washington Press, 1996.

[16] Chuan, R. L., Woods, D. C. and M. P. McCormick: Characterisation of aerosols from eruptions of Mount St.Helens, *Science*,**211**, 830–832, 1981.

[17] Constantine, E. K., Bluth, G. J. S., and Rose, W. I.: TOMS and AVHRR sensors applied to drifting volcanic clouds from the August 1991 eruptions of Cerro Hudson, AGU Monograph 116– Remote Sensing of Active Volcanism, Ed. by P. Mouginis-Mark, J. Crisp and J. Fink, pp. 45–64, 2000.

[18] Clerbaux, C., Turquety, S., Hadji-Lazaro, J., George, M., Boynard, A, Pommier, M, Coheur, P.-F., Hurtmans, D., Wespes, C., Razavi, A., and Herbin, H.: Monitoring of volcanic SO_2 using thermal infrared IASI/METOP sounders (TES, IASI), paper presented at the Support to Aviation Control Service meeting, Toulouse, 26-27 November 2007.

[19] Damoah, R., Spichtinger, N., Forster, C., James, P., Mattis, I., Wandinger, U., Beirle, S., and Stohl, A.: Around the world in 17 days – hemispheric-scale transport of forest fire smoke from Russia in May 2003, Atmos. Chem. Phys., 4, 1311–1321, 2004.

[20] Davies, M. A., and Rose, W. I.,: Evaluating GOES imagery for volcanic cloud observations at the Soufrière Hills volcano, Montserrat, *EOS Trans.*, AGU, **79**, 505–507, 1998.

[21] Draxler, R. R., and Rolph, G. D.: HYSPLIT (Hybrid Single-Particle Lagrangian Integrated Trajectory) model access via NOAA ARL READY Website (http://www.arl.noaa.gov/ready/hysplit4.html), NOAA Air Resources Laboratory, Silver Spring, MD, USA, 2003.

[22] ECMWF (White, P. W., ed.): IFS Documentation, ECMWF, Reading, UK, 2002, available online at `http://www.ecmwf.int`

[23] Eckhardt, S., Prata, A. J., Seibert, P., Steibel, K., and Stohl, A.: Estimation of the vertical profile of sulfur dioxide injection into the atmosphere by a volcanic eruption using satellite column measurements and inverse transport modeling, Atmos. Chem. Phys., 2008.

[24] Eckhardt, S., Breivik, K., Man, S., and Stohl, A.: Record high peaks in PCB concentrations in the Arctic atmosphere due to long-range transport of biomass burning emissions, Atmos. Chem. Phys., 7, 4527–4536, 2007.

[25] Eisinger, M. and Burrows, J.P.: Tropospheric sulfur dioxide observed by the ERS-2 GOME instrument, Geophys. Res. Lett., 25(22), 4177–4180, 1998.

[26] Ellrod, G. P., Connell, B. H., and Hillger, D. W.: Improved detection of airborne volcanic ash using multispectral infrared satellite data, J. Geophys. Res., 108, D12, 4356, doi:10.1029/2002JD002802, 2003.

[27] Emanuel, K. A., and Živković-Rothman, M.: Development and evaluation of a convection scheme for use in climate models, J. Atmos. Sci., 56, 1766–1782, 1999.

[28] ESCAP: Review of Developments in transport in Asia and the Pacific 2005, United Nations Publ., No. E.06.II.F.9, ST/ESCAP/2392, 172pp., 2005.

[29] Evans, B. T. N.: An interactive program for estimating extinction and scattering properties of most particulate clouds, *Department of Defence Report* **MRL-R-1123**, Defence Science and Technology Organisation, Materials Research Laboratory, P.O. Box 50, Ascot Vale, Victoria 3032, Australia, 1988.

[30] Eyers, C. J., Norman, P., Middel, J., Michot, S., Atkinson, K., and Christou, R. A.: AERO2k Global aviation emissions inventories for 2002 and 2025, European Commission Contract, No. G4RD-CT-2000-00382, QINETIQ/04/0113, 144pp., 2004.

[31] Fleming, E.L., Chandra, S., Shoeberl, M.R., and Barnett, J.J.: Monthly mean global climatology of temperature, wind, geopotential height and pressure for 0-120 km, National Aeronautics and Space Administration, Technical Memorandum 100697, Washington, D.C., 1998.

[32] Forster, C., Stohl, A., and Seibert, P.: Parameterization of convective transport in a Lagran-gian particle dispersion model and its evaluation, J. Appl. Met. Clim., 46, 403–422, 2007.

[33] Gangale, G., Prata, A. J., and Clarisee, L.,: The infrared signature of volcanic ash determined from high-spectral resolution satellite measurements, *Re,. Sensing Environ.*, *Accepted*, 2009.

[34] Hanstrum, B.N., and Watson, A.S.: A case study of two eruptions of Mount Galunggung and an investigation of volcanic eruption cloud characteristics using remote sensing techniques, Aust. Met. Mag., 31, 131–177, 1983.

[35] Heffter, J. L.: Volcanic ash model verification using a Klyuchevskoi eruption, Geophys. Res. Lett., 23, 1489–1492, 1996.

[36] Hillger, D. W. and Clark, J. D.: Principal component image analysis of MODIS for volcanic ash. Part I: Most important bands and implications for future GOES imagers, J. Appl. Meteorol., 41, 985–1001, 2002.

[37] Hillger, D. W. and Clark, J. D.: Principal component image analysis of MODIS for volcanic ash. Part II: Simulation of current GOES and GOES-M imagers, J. Appl. Meteorol., 41, 1003–1010, 2002.

[38] Hobbs, P. V., Radke, L. F., Eltgroth, M. W., and Hegg, D. A.: Airborne studies of the emissions from the volcanic eruptions of Mount St.Helens, *Science*, **211**, 816–818, 1981.

[Hofman and Rosen] Hofmann, D. J., and Rosen, J. M.: Balloonborne particle counter observations of the El Chichón aerosol layers in the 0.01–1.8 μm radius range, *Geofisica International*, **23**, 155–185, 1984.

[39] Holasek, R. E., and W. I. Rose: Anatomy of 1986 Augustine Volcano eruptions as recorded by multispectral images processing of digital AVHRR weather satellite data, Bull. Volc., 53, 42–435, 1991.

[40] Holasek, R. E., Woods, A. W. and Self, S.: Experiments on gas-ash separation processes in volcanic umbrella clouds, J. Volcanol. Geotherm. Res., 70, 169–181, 1996.

[41] Ivlev, L. S., and Popova, S. I.: The complex refractive indices of substances in the atmospheric-aerosol dispersed phase, *Atmospheric Oceanic Physics*, **9**(10), 587–591, 1973.

[42] King, M. D., Harshvardhan, and Arking, A.: A model of the radiative properties of the El Chichón stratospheric layer, *J. Climate Appl. Meteorol.*, **23**, 1121–1137, 1984.

[43] Krotkov, N. A., Carn, S. A., Krueger, A. J., Bhartia, P. K., and Yang, K.: Band residual difference algorithm for retrieval of SO_2 from the Aura Ozone Monitoring Instrument (OMI), IEEE Trans. Geosci. Remote Sens., 44(5), 1259–1266, 2006.

[44] Krueger, A. J.: Sighting of El Chichon sulfur dioxide clouds with the Nimbus 7 Total Ozone Mapping Spectrometer, Science, 220, 1377–1379, 1983.

[45] Krueger, A. J., Walter, L. S., Bhartia, P. K., Schnetzler, C. C., Krotkov, N. A., Sprod, I., and Bluth, G. J. S.: Volcanic sulfur dioxide measurements from the total ozone mapping spectrometer instruments, J. Geophys. Res., 100(D7), 14,057–14,076, 1995.

[46] Krueger, A. J., Schaefer, S. J., Krotkov, N., Bluth, G.J.S., and Baker, S.: Ultraviolet remote sensing of volcanic emissions, Remote Sensing of Active Volcanism, Geophys. Monogr. Ser., 116, Ed. P. J. Mouginis-Marks, J. A. Crisp and J. H. Fink,, 2543, AGU, Washington, D. C., 2000.

[47] Malingreau, J. -P. and Kaswanda: Monitoring volcanic eruptions in Indonesia using weather satellite data: The Colo eruption of July 28, 1983, J. Volcanol. Geothermal Res., 27(1–2), 179–194, 1986.

[48] Manins, P. C.: Cloud heights and stratospheric injections resulting from a thermonuclear war, *Atmos. Environ.*, **19**(8), 1245–1255, 1985.

[49] Mankin, W. G., Coffey, M. T., and Goldman, A.: Airborne observations of SO_2, HCl, and O_3, in the stratospheric plume of the Pinatubo volcano in July 1991, Geophys. Res. Lett., 19, 179–182, 1992.

[50] Masuda, K., and T. Takashima: Deriving cirrus information using the visible and near-ir channels of the future NOAA-AVHRR radiometer, *Remote Sens. Environ.*, **31**:65—81, 1990.

[51] Matson, M.: The 1982 El Chichon volcano eruptions–a satellite perspective, J. Volcanol. Geotherm. Res., 23, 1–10, 1984.

[52] Menke, W.: Geophysical Data Analysis: Discrete Inverse Theory. 260 pp., Academic Press, Orlando, 1984.

[53] Miller, T. P., and Casadevall, T. J.: Volcanic ash hazards to aviation, Encyclopedia of Volcanoes, edited by H. Sigurdsson, B. Houghton, S. R. McNutt, H. Ryman, and J. Stix, Academic Press, San Diego, pp. 915–930, 1999.

[54] Mosher, F. R.: Four channel volcanic ash detection algorithm, Preprint Volume, 10th Conf. Satellite Meteorol. and Oceanography, 9–14 January, 2000, Long Beach, California, 457–460, 2000.

[55] Mossop, S. C.: Volcanic dust collected at an altitude of 20 km, *Nature*, **203**, No. 4947, 824–827, 1964.

[56] Newell, R. E., and Deepak, A. (*Eds.*): Mount St. Helens eruptions of 1980: Atmospheric effects and potential climate impact, *NASA Workshop Report*, **NASA SP-458**, Sciientific and Technical Information Branch, NASA, Washinton, D. C., 119pp, 1982.

[57] Oberhuber, J. M., Herzog, M., Graf, H.-F., and Schwanke, K.: Volcanic plume simulation on large scales, J. Volcan. Geoth. Res., 87, 29–53, 1998.

[58] Pavolonis, M. J., Feltz, W. F., Heidinger, A. K., and Gallina, G. M.: A daytime complement to the reverse absorption technique for improved automated detection of volcanic ash, J. Atmos. Oceanic Technol., 23, 1422–1444, 2006.

[59] Pergola, N., Tramutoli, V., Marchese, F., Scaffidi, I., and Lacav, T.: Improving volcanic ash cloud detection by a robust satellite technique, Rem. Sens. Environ., 90, 1–22, 2004.

[60] Pieri, D., Ma, C., Simpson, J. J., Hufford, G., Grindle, T., and Grove, C.: Analyses of in-situ airborne ash from the February 2000 eruption of Hekla volcano, Iceland, Geohpys. Res. Lett., 29(16), 10.1029/2001GL013688, 2002.

[61] Pollack, J. B., Toon, O. B., and Khare, B. N.: Optical properties of some terrestrial rocks and glasses, *Icarus*, **19**, 372–389, 1973.

[62] Prata, A. J.: Observations of volcanic ash clouds using AVHRR-2 radiances. Int. J. Remote Sensing, 10(4-5), 751-761, 1989a.

[63] Prata., A. J.: Radiative transfer calculations for volcanic ash clouds, Geophys. Res. Lett., 16(11), 1293-1296, 1989b.

[64] Prata, A. J., Bluth, G. J. S., Rose, W. I., Schneider, D. J., and Tupper, A. C.: Comments on Failures in detecting volcanic ash from a satellite-based technique Rem. Sensing Environ., 78, 341–346, 2001.

[65] Prata, A. J. and Grant, I. F.: Retrieval of microphysical and morphological properties of volcanic ash plumes from satellite data: Application to Mt. Ruapehu, New Zealand., Quart. J. Roy. Meteorol. Soc., 127(576B), 2153–2179, 2001.

[66] Prata, A. J.,Rose, W. I., Self, S., and D. M., O'Brien: Global, long-term sulphur dioxide measurements from TOVS data: A new tool for studying explosive volcanism and climate, Volcanism and the Earth's Atmosphere, Geophys. Monograph 139, AGU, 75–92, 2003.

[67] Prata, A. J. and Barton, I. J.: Detection and discrimination of volcanic ash clouds by infrared radiometry – I: theory. In: Casadevall, T. J., editor. Volcanic Ash and aviation safety: proceedings of the first International Symposium on Volcanic Ash and Aviation Safety; Seattle, Wash. Washington, D.C.: U.S. G.P.O., *U.S. Geological Survey bulletin, 1994.*
2047*, 305-311.*

[68] Prata, A. J. and Bernardo, C.: Retrieval of volcanic SO_2 column abundance from Atmospheric Infrared Sounder data, J. Geophys. Res, 112, D20204, doi:10.1029/2006JD007955, 2007.

[69] Prata, A. J., Carn, S. A., Stohl, A., and Kerkmann, J.: Long range transport and fate of a stratospheric volcanic cloud from Soufriere Hills volcano, Montserrat, Atmos. Chem. Phys., 7, 5093–5103, 2007.

[70] Prata, A. J., and Kerkmann, J.: Simultaneous retrieval of volcanic ash and SO_2 using MSG-SEVIRI measurements, Geophys. Res. Lett., 34, L05813, doi:10.1029/2006GL028691, 2007.

[71] Press, W. H., Flannery, B. P., Teukolsky, S. A., and Vetterling, W. T.: Numerical Recipes, *Cambridge University Press*, 818pp, 1986.

[72] Przedpelski, Z. J., and Casadevall, T. J.: Impact of volcanic ash from 15 December 1989 Redoubt volcano eruption on GE CF6-80C2 turbofan engines, *In Volcanic ash and aviation safety: Proc. of the First International Symposium on Volcanic Ash and Aviation Safety*, US. Geological Survey Bulletin **2047**, 129–135, Seattle, Washington, July, 1991, 1994.

[73] Richardson, A. J.: El Chichon volcanic ash effects on atmsopheric haze measured by NOAA-7 AVHRR data, Remote Sens. Environ, 16, 157–164, 1984.

[74] Richter, A., Wittrock, F. and Burrows, J.P.: SO_2 measurements with SCIAMACHY, Proceedings of the First Converence on Atmospheric Science, 8–12 May 2006, Frascati, Italy, ESA publication SP-628, 2006.

[75] Rose, W. I., Delene, D. J., Schneider, D. J., Bluth, G. J. S., Kruger, A. J., Sprod, I., McKee, C., Davies, H. L., and Ernst, G. J.: Ice in the 1994 Rabaul eruption: Implications for volcanic hazard and atmospheric effects, Nature, 375, 477-479, 1995.

[76] Sawada, Y: Study on analysis of volcanic eruptions based on eruption cloud image data obtained by the Geostationary Meteorological Satellite (GMS), Technical Reports of the Meteorological Research Institue, 22, 335 pp., 1987.

[77] Sawada, Y.: Detection of explosive eruptions and regional tracking of volcanic ash clouds with geostationary meteorological satellites (GMS), Monitoring and Mitigation of Volcano Hazards, Scarpa, R. and Tilling, RI. (eds.), Springer-Verlag Berlin Heidelberg, pp. 299–314, 1996.

[78] Schneider, D. J., Rose, W. I., and Kelley, L.: Tracking of 1992 eruption clouds from Crater Peak of Mount Spurr volcano, Alaska, using AVHRR, U. S. Geol. Survey Bull., 2139, 27–36, 1995.

[79] Schneider, D. J., Rose, W. I., Coke, L. R., and Bluth, G. J. S: Early evolution of a stratospheric volcanic eruption cloud as observed with TOMS and AVHRR, J. Geophys. Res., 104(D4), 4037-4050, 1999.

[80] Seibert, P.: Inverse modelling of sulfur emissions in Europe based on trajectories, In: Inverse Methods in Global Biogeochemical Cycles, edited by Kasibhatla, P., Heimann, M., Rayner, P., Mahowald, N., Prinn, R. G., and Hartley, D. E., pp. 147-154, Geophysical Monograph 114, American Geophysical Union, ISBN 0-87590-097-6, 2000.

[81] Seibert, P.: Inverse modelling with a Lagrangian particle dispersion model: application to point releases over limited time intervals, In: Air Pollution Modeling and its Application XIV, edited by Schiermeier, F.A. and Gryning, S.-E., pp. 381-389, Kluwer Academic Publ., 2001.

[82] Sehmel, G. A.: Ambient airborne solids concentrations including volcanic ash at Hanford, Washington, sampling sites subsequent to the Mount St Helens eruption, In *Atmospheric effects and potential climatic impact of the 1980 eruptions of Mount St Helens, Deepak (Ed.)*, **NASA Conference Publ. 2240**, NASA Scientific and Tech. Information Branch, 283–292, 1982.

[83] Simkin T. and Seibert, L.: Volcanoes of the world, 2nd Edn. Geoscience Press, Tucson, Arizona, 1994.

[84] Simpson, J. J., Hufford, G., Pieri, D., and Berg, J.: Failures in detecting volcanic ash from a satellite-based technique, Remote Sens. Environ., 72: 191–217, 2000.

[85] Simpson, J. J., Hufford, G., Pieri, D., Servranckx, R. and Berg, J.: The February 2001 Eruption of Mount Cleveland, Alaska: Case Study of an Aviation Hazard, Weather and Forecasting, 17, 691–704, 2002.

[86] Sokolik, I. N., and Toon, O., B.: Incorporation of mineralogical composition into models of the radiative properties of mineral aerosol from UV to IR wavelengths, *J. Geophys. Res.*, **104** (D8), 9423–9444, 1999.

[87] Stamnes, K. and Swanson, R. A.: A new look at the discrete ordinates method for radiative transfer calculations in anisotropically scattering atmospheres, *J. Atmos. Sci.*, **38**, 387–399, 1981.

[88] Stohl, A., Hittenberger, M., and Wotawa, G.: Validation of the Lagrangian particle dispersion model FLEXPART against large scale tracer experiment data, Atmos. Environ., 32, 4245–4264, 1998.

[89] Stohl, A., and Thomson, D. J.: A density correction for Lagrangian particle dispersion models, Boundary-Layer Meteorol., 90, 155–167, 1999.

[90] Stohl, A., Forster, C. Eckhardt, S., Spichtinger, N., Huntrieser, H., Heland, J., Schlager, H., Wilhelm, S., Arnold, F., and Cooper, O.: A backward modeling study of intercontinental pollution transport using aircraft measurements, J. Geophys. Res., 108, 4370, doi:10.1029/2002JD002862, 2003.

[91] Stohl, A., Forster, C., Frank, A., Seibert, P., and Wotawa, G.: Technical note: The Lagrangian particle dispersion model FLEXPART version 6.2., Atmos. Chem. Phys., 5, 2461–2474, 2005.

[92] Stunder, B. J. B., Heffter, J. L., and Draxler, R. R.: Airborne volcanic ash forecast area reliability, Wea. Forecasting, 22, 1132-1139, 2007.

[93] Textor, C., Graf, H. F., Herzog, M., and Oberhuber, J. M.: Injection of gases into the stratosphere by explosive volcanic eruptions, J. Geophys. Res., 108, 4606, doi:10.1029/2002JD002987, 2003.

[94] Thomas, W., Erbertseder, T., Ruppert, T., Van Roozendael, M., Verdebout, J., Balis, D., Meleti, C. and Zerefos, C.: On the retrieval of volcanic sulfur dioxide emissions from GOME backscatter measurements, J. Atm. Chem., 50, 295–320, doi:10.1007/s10874-005-5079-5, 2004.

[95] Tupper, A., Carn, S. A., Davey, J., Kamada, Y., Potts, R. J., Prata, A. J., and Tokuno, M.: An evaluation of volcanic cloud detection techniques during recent significant eruptions in the western Ring of Fire, Remote Sens. Environ., 91, 27–46, 2004.

[96] Van Geffen, J., Van Roozendael, M., Di Nicolantonio, W., Tampellini, L., Valks, P., Erbetseder, T. and Van der A, R.: Monitoring of volcanic activity from satellite as part of GSE PROMOTE, Proceedings of the First Converence on Atmospheric Science, 8–12 May 2006, Frascati, Italy, ESA publication SP-628, 2007.

[Volz 1973] Volz, F. E.: Infrared optical constants of ammonium sulfate, Sahara dust, volcanic pumice, and flyash, *Appl. Opt.*, **12**(3), 564–568, 1973.

[97] Wang, X., Boselli, A., D'Avino, L., Pisani, G., Spinelli, et al.: Volcanic dust characterization by EARLINET during Etna's eruptions in 2001-2002, Atmos. Environ., 42, 893-905, 2008.

[98] Watkin, S.C.: The application of AVHRR data for the detection of volcanic ash in a Volcanic Ash Advisory Centre, Meteorol. Appl., 10, 301–311, 2003.

[99] Wei,C.-F., Larson, S.M., Pattena, K.O., Wuebbles, D.J.: Modeling of ozone reactions on aircraft-related soot in the upper troposphere and lower stratosphere, Atmos. Environ., 35, 6167–6180, 2001.

[100] Wen, S., and Rose, W. I.: Retrieval of sizes and total masses of particles in volcanic clouds using AVHRR bands 4 and 5, J. Geophys. Res., 99(D3), 5421-5431, 1994.

[101] Wesely, M. L. and Hicks, B. B.: Some factors that affect the deposition rates of sulfur dioxide and similar gases on vegetation. J. Air Poll. Contr. Assoc., 27, 1110–1116, 1977.

[102] Witham, C.S., Hort, M.C., Potts, R., Servranckx, R, Husson, P. and Bonnardot, F.: Comparison of VAAC atmospheric dispersion models using the 1 November 2004 Grimsvtn eruption, Meteorol. Appl., 14, 27–38, 2007.

[103] Winker D. M., Hunt, W. H., and McGill, M. J: Initial performance assessment of CALIOP, Geophys. Res. Lett., 34, L19803, doi:10.1029/2007GL030135, 2007.

[104] Wotawa, G., De Geer L.E., Denier P, et al.: Atmospheric transport modelling in support of CTBT verification – overview and basic concepts, Atmos. Environ. 37, 2529–2537, 2003.

[105] Yu, T-X, and Rose, W. I.: Retrieval of sulfate and silicate ash masses in young (1 to 4 days old) eruption clouds using multiband infrared HIRS/2 data, In *AGU Monograph on Remote Sensing of Active Volcanism*, 1999.

[106] Yu, T., Rose, W. I. and Prata, A. J.: Atmospheric correction for satellite-based volcanic ash mapping and retrievals using split window IR data from GOES and AVHRR, J. Geophys. Res., 107(D16), 4311, 10.1029/2001JD000706, 2002.

Chapter 8

Appendix I: Acronyms

ASTER	Advanced Spaceborne Thermal Emission and Reflection Radiometer
AIRS	Atmospheric InfraRed Spectrometer
ATSR	Along-Track Scanning Radiometer
AVHRR	Advanced Very High Resolution Radiometer
CALIPSO	Cloud-Aerosol Lidar and Infrared Pathfinder Satellite Observations
DOAS	Differential Optical Absorption Spectroscopy
GOES	Geosynchronous Orbiting Environmental Satellite
GOME	Global Ozone Monitoring Experiment
HIRS	High resolution InfraRed Sounder
HYSPLIT	HYbrid Single-Particle Lagrangian Integrated Trajectory
IASI	Infrared Atmospheric Sounding Interferometer
IR	InfraRed
MetOP	Operational meteorological satellite
MLS	Microwave Limb Sounder
MODIS	Moderate Resolution Imaging Spectroradiometer
MSG	Meteosat Second Generation
MUT	Mid and Upper- Troposphere
NOAA	National Oceanographic and Atmospheric Administration
OMI	Ozone Monitoring Instrument
PUFF	Volcanic Ash Tracking Model
SCIAMACHY	SCanning Imaging Absorption SpectroMeter for Atmospheric ChartographY
SEVIRI	Spinning Enhanced Visible and InfraRed Imager
TIROS	Television and Infrared Orbiting Satellite
TOMS	Total Ozone Mapping Spectrometer
UTLS	Upper Troposphere Lower Stratosphere
UV	Ultra-Violet
VISSR	Visible and Infrared Spin Stabilised Radiometer